Geochemistry, Geophysics, Geosystems

RESEARCH ARTICLE
10.1029/2019GC008354

Special Section:
Magmatic and volcanic processes in continental rifts

Key Points:
- Steep nodal planes of earthquake focal mechanisms correspond to projections of border and intrabasinal faults to depths of 25 km
- Extension direction across Rungwe volcanic province and Malawi rift is ENE, refuting interpretations of a NW-SE transform fault system
- Low *b*-value, fault lengths >100 km, seismogenic layer 25-30 km, and aseismic deformation suggest that infrequent M>7.5 earthquakes are possible

Supporting Information:
- Supporting Information S1

Correspondence to:
C. J. Ebinger,
cebinger@tulane.edu

Citation:
Ebinger, C. J., Oliva, S. J., Pham, T.-Q., Peterson, K., Chindandali, P., Illsley-Kemp, F., et al. (2019). Kinematics of active deformation in the Malawi rift and Rungwe Volcanic Province, Africa. *Geochemistry, Geophysics, Geosystems*, *20*. https://doi.org/10.1029/2019GC008354

Received 26 MAR 2019
Accepted 5 JUL 2019
Accepted article online 22 JUL 2019

Kinematics of Active Deformation in the Malawi Rift and Rungwe Volcanic Province, Africa

C. J. Ebinger[1], Sarah Jaye Oliva[1], Thi-Quan Pham[1], Katherine Peterson[2], Patrick Chindandali[3], Finnigan Illsley-Kemp[4], Connor Drooff[5], Donna J. Shillington[6], Natalie J. Accardo[7], Ryan J. Gallacher[1], J. Gaherty[6], Andrew A. Nyblade[7], and Gabriel Mulibo[8]

[1]Department of Earth and Environmental Sciences, Tulane University, New Orleans, LA, USA, [2]Radiant Solutions, Herndon, VA, USA, [3]Malawi Geological Survey, Zomba, Malawi, [4]School of Geography, Environment, and Earth Sciences, Victoria University of Wellington, Wellington, New Zealand, [5]Department of Earth and Environmental Sciences, Michigan State University, East Lansing, MI, USA, [6]Lamont-Doherty Earth Observatory, Columbia University, Palisades, NY, USA, [7]Department of Geosciences, Penn State University, College Park, PA, USA, [8]Department of Geology, University of Dar-es-Salaam, Dar es Salaam, Tanzania

Abstract Although the deep, wide basins of the Western rift, Africa, have served as analogues for the evolution of half-graben basins, the geometry and kinematics of the border, intrabasinal, and transfer fault systems have been weakly constrained. Despite the >100-km-long fault systems bounding basins, little was known of seismicity patterns or the potential for $M > 7.5$ earthquakes. Using our new local earthquake database from the 2013-2015 Study of Extension and maGmatism in Malawi aNd Tanzania (SEGMeNT) seismic array (57 onshore, 32 lake-bottom stations) and TANGA14 (13 stations), we examine the kinematics and extension direction of the Rungwe Volcanic Province and northern Malawi rift. We relocated earthquakes using a new 1-D velocity model and both absolute and double-difference relocation methods. Local magnitudes of 1,178 earthquakes within the array are $0.7 < M_L < 5.2$ with a *b*-value 0.77 ± 0.03, and magnitude of completeness M_L 1.9. Focal mechanism solutions for 63 earthquakes reveal predominantly normal and oblique-slip motion, and full moment tensor solutions for M_L 4.5, 5.2 earthquakes have centroid depths within 2 km of catalog depths. The preferred nodal planes dip more than 40° from surface to >25-km depths. Extension direction from local earthquakes and source mechanisms of teleseismically detected earthquakes are approximately N58°E and N65°E, respectively, refuting earlier interpretations of a NW-SE transform fault system. The low *b*-value indicating strong coupling across crustal-scale border faults, border fault lengths >100 km, and evidence for aseismic deformation together indicate that infrequent $M > 7.5$ earthquakes are possible within this cratonic rift system.

1. Introduction

Asymmetric (half-graben) extensional basins bounded by large offset border faults are ubiquitous in early stage and failed continental rift zones, yet the time-space evolution of border and intrabasinal faults remain debated, in part owing to the lack of constraints on lower crustal strain patterns (e.g., Lavier & Buck, 2002; Olive et al., 2014). The border fault length and depth, and basin width are in large part controlled by the strength of the lithosphere, which varies with composition, geothermal gradient, and hydration state (e.g., Braun & Beaumont, 1989; Weissel & Karner, 1989). Cratonic rifts are extensional zones in lithosphere that has been stable for >1 Ga and may include Archaean cratons, as in East Africa. The long, large displacement faults bounding wide basins with broad uplifted flanks can be simulated by extension of mechanically strong crust and border faults that penetrate to the lower crust (e.g., Ebinger et al., 1991; Weissel & Karner, 1989), but few detailed studies of seismicity are available to evaluate: Is cratonic crust in extension brittle throughout its entirety?

Seismicity patterns in active rift basins provide important constraints on the mechanical properties of the lithosphere, as well as the kinematics of discrete border fault systems, and their along-axis linkage patterns. In rift sectors lacking magmatism, the seismogenic layer thickness is a proxy for the short time-scale strength of the elastic crust (e.g., Watts & Burov, 2003). Magma intrusion and eruption processes superpose additional time and length scales to rift strain patterns (e.g., Ebinger & Casey, 2001). Heat transfer and metasomatic processes reduce plate strength adjacent to intrusions, also localizing strain (e.g., Buck, 2004; Burov et al., 2003; Wang et al., 2015).

Rift zones in cratonic regions where the seismogenic layer thickness may span the entire crust, such as in the East African rift system, provide insights into strain distribution in magmatic and weakly magmatic rift zones (e.g., Ebinger et al., 2017; Gupta, 1992; Yang & Chen, 2010). Earthquake distributions, magnitudes, and source mechanisms from the seismically and volcanically active Malawi rift and Miocene-Recent Rungwe Volcanic Province (RVP), Africa, provide critical constraints on fault kinematics and crustal rheology during rifting of cratonic lithosphere. Extensive crust and mantle imaging in this area has been undertaken as part of the Study of Extension and maGmatism in Malawi aNd Tanzania (SEGMeNT) project and reanalyses of earlier data (Accardo et al., 2017; Borrego et al., 2018; Grijalva et al., 2018; McCartney & Scholz, 2016; Tepp et al., 2018). The SEGMeNT study area includes the site of a 2-week-long sequence of nine Mw 4.9-6.0 earthquakes in 2009 (Biggs et al., 2010; Gaherty et al., 2019; Kolawole et al., 2018a, 2018b), and a 2014 Mw 5.2 earthquake recorded by the SEGMeNT array. Rift kinematics in the RVP and northern Malawi rift have been debated, with NW-SE extension, NW-SE transform opening, ENE-extension, and Quaternary stress field rotation interpreted (e.g., Chorowicz et al., 2005; Mortimer et al., 2007; Delvaux & Barth, 2010; Stamps et al., 2018).

Our objectives are to evaluate half-graben basin models by determining the depth distribution and kinematics of earthquakes beneath two distinct rift segments with opposing asymmetries and beneath their uplifted flanks, and between areas with and without surface evidence of magmatism. The half-graben and their uplifted flanks form over many earthquake cycles along border and intrabasinal faults, and the SEGMeNT array captures a snapshot of strain patterns. We compare the time-space patterns of earthquakes relocated using double-difference methods with border, intrabasinal, and transfer faults, and compare active and time-averaged strain patterns. Data from the 2013-2015 SEGMeNT deployment, consisting of 57 seismometers in the RVP and Malawi rift, as well as 6 broadband and 28 short-period ocean bottom seismometers (OBS), combined with data from the TANGA14 (Hodgson et al., 2017) and Malawi Geological Survey national network are used (Figure 1). Seismicity patterns from this approximately 2-year deployment are compared with longer-term information from historic and instrumentally recorded earthquakes detected at teleseismic distances (e.g., Ambraseys, 1991; Craig et al., 2011; Yang & Chen, 2010). SEGMeNT data are used to develop a new 1-D velocity model, a local magnitude scaling with new estimates of seismic attenuation, and *b*-value using our new magnitude scaling.

2. Tectonic Background

The RVP and northern Malawi rift zone lie along the southeastern edge of the dynamically supported East African plateau (e.g., Lithgow-Bertelloni & Silver, 1998; Behn et al., 2004; Figure 1). North and west of the Malawi rift, elevations increase and active faulting is distributed across a zone at least 350 km in breadth, including the thick Bangweulu craton (Lavayssière et al., 2019). The broad uplifted plateau, its corresponding negative Bouguer gravity anomalies, low upper mantle seismic velocities, and the geochemistry of eruptive volcanic products have been cited as evidence for one or more mantle plumes (e.g., Halldórsson et al., 2014; Mulibo & Nyblade, 2013; Nyblade & Robinson, 1994). Localized alkali and carbonatitic lavas showing extensive metasomatism characterize the RVP, and other Western rift magmatic provinces, indicating melting of a metasomatized mantle lithosphere at depths ~85 km (e.g., Barry et al., 2013; Furman, 1995; Lloyd et al., 1985).

The Malawi rift system formed in the Irumidian, Ubendian, and Pan-African (Proterozoic) orogenic belts between the thick lithosphere of the Tanzanian craton and Bangweulu cratons (e.g., Fishwick & Bastow, 2011; Fritz et al., 2013; Boniface & Appel, 2018; Grijalva et al., 2018; Figure 1). The Proterozoic crust shows a variety of regional strain fabrics and structural orientations, ranging from NE, NNW to NW, to N-S along the eastern side of the Malawi rift (e.g., Fritz et al., 2013). Mantle imaging reveals high velocities beneath the Bangweulu and Tanzania cratons, and low *P* and *S* wave velocity zones beneath the RVP and northernmost Malawi rift, although spatial gaps remain in our knowledge of the Western rift (e.g., Mulibo & Nyblade, 2013; O'Donnell et al., 2015; Accardo et al., 2017; Grijalva et al., 2018).

Parts of the study area were affected by Permian-Jurassic (Karroo) rifting, with some basins containing up to 2 km of Permian strata (Stockley, 1931; Kaaya, 1992; Figure 2). These include the southern Rukwa and Usangu

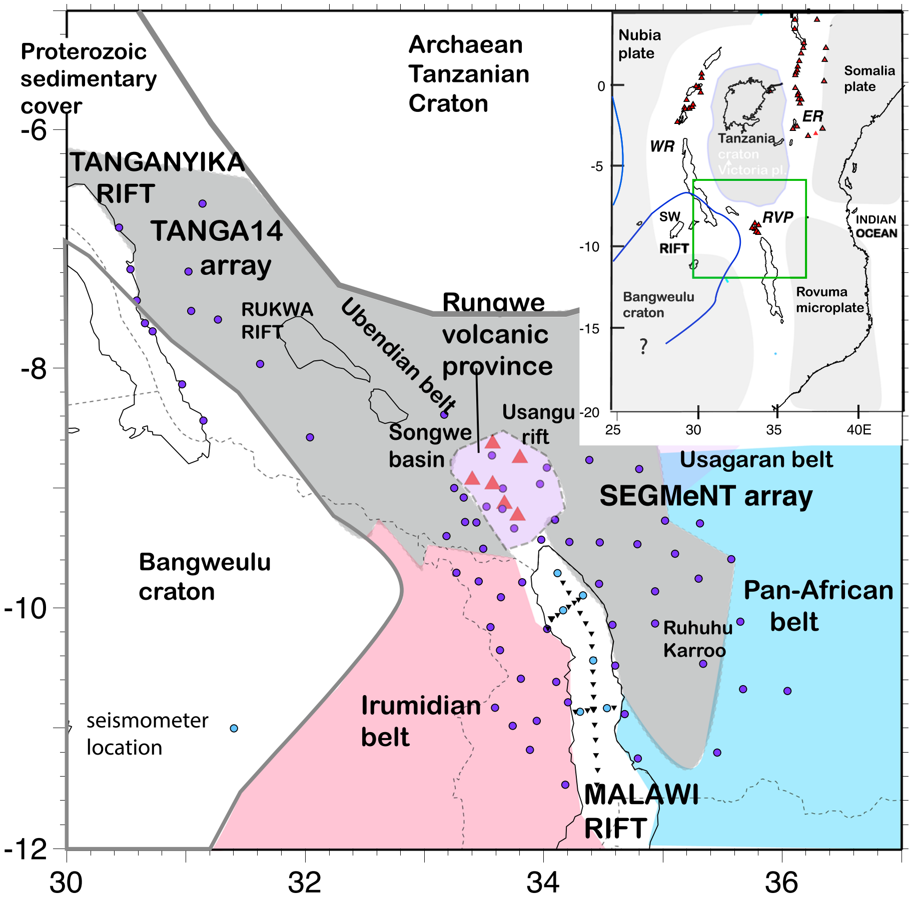

Figure 1. Inset: Location of Tanganyika-Rukwa-Malawi rift zone and Rungwe Volcanic Province (RVP) with respect to stable plates (grey shading, after Stamps et al., 2018, and Lavayssière et al., 2019) and large lakes of the East African rift zone. The red triangles are Holocene volcanoes in the RVP. Main: Hill-shaded relief with location of seismic stations relative to fault bounded rift basins and major tectonic units, including the 2014-2015 TANGA14 array (Hodgson et al., 2017). Archaean Bangweulu and Tanzania cratons outlined by grey lines. Grey: Paleoproterozoic Ubendian orogenic belt. Rose color: Mesoproterozoic Irumidian orogenic belt. Purple: Mesoproterozoic Usagaran orogenic belt. Blue: Neoproterozoic Pan-African orogenic belt (after Fritz et al., 2013). Violet: Extrusive lavas and volcaniclastic rocks of the RVP after Fontijn et al. (2012). Karroo rifts are Permo-Triassic rift basins shown with green colors in Figure 2. The circles denote onshore seismic stations (purple); the inverted triangles (short period) and circles (broadband) indicate lake-bottom seismometers used in this study.

basins (e.g., Mbede, 2002; Harper et al., 1999; Figures 1 and 2). Eastward dipping Cretaceous sedimentary strata on the western side of the North (Karonga) Basin suggest a second, poorly understood period of extensional faulting (e.g., Ring, 1994). Permo-Triassic and Cretaceous faults strike NNE to NE throughout the region, excluding the NW-trending Rukwa rift zone (e.g., Castaing, 1991; Ring, 1994; Figure 2).

The Malawi rift is structurally segmented along its length into a series of fault-bounded half-graben basins containing up to 5 km of sedimentary strata (e.g., Accardo et al., 2018; Ebinger et al., 1989; McCartney & Scholz, 2016). The SEGMeNT project encloses the northern two basins: the eastward tilted North basin and the westward-tilted Central basin that are bounded by the Livingstone and Usisya border faults, respectively (Figure 2). A faulted relay ramp links the two rift segments, both of which may be underlain by Karroo and Cretaceous strata (Accardo et al., 2018). It also includes the Songwe basin in the southern Rukwa rift, and the NE trending Usangu basin that contains Karroo and Miocene-Recent strata (Mbede, 2002; Harper et al., 1999). The northern end of the North basin and western side of the Usangu basin are covered by ~17 Ma to Recent lavas of the RVP (RVP; Rasskazov et al., 2001; Mesko et al., 2014). Some of the eruptive centers are oriented along NNW striking transfer fault zones linking the Songwe and Livingstone border faults (Ebinger et al., 1989; Fontijn et al., 2012).

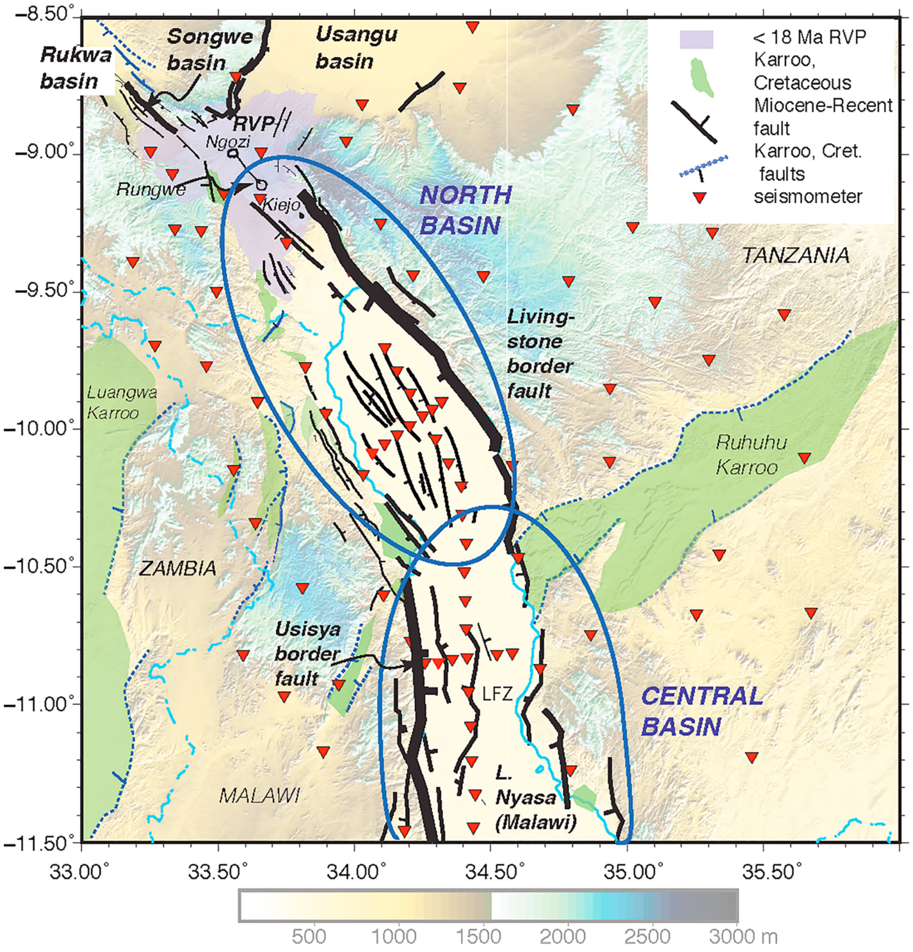

Figure 2. Study of Extension and maGmatism in Malawi aNd Tanzania (SEGMeNT) seismic arrays (inverted red triangles) -Recent rift faults, and hill-shaded rift topography. Lakelevel is 477 m. Onshore faults from Crossley (1984), Ebinger et al. (1993), Fontijn et al. (2012), Fritz et al. (2013), and Kolawole et al. (2018b); offshore from McCartney and Scholz (2016). North and Central basins of the Malawi rift are enclosed in blue ellipses. The Malawi rift transects fault-bounded Permian to Palaeogene basin strata (green shading). Major Permian-Palaeogene structures (dotted lines). Purple is Miocene-Recent Rungwe Volcanic Province (RVP) with three volcanoes active in the Holocene: Ngozi, Rungwe, and Kiejo. Rukwa basin contains Mesozoic-Recent strata. LFZ is Lipichili fault zone.

Multiple hypotheses for the kinematics of rifting in the RVP and Northern Malawi rift zone have been proposed owing to the junction of the NNW striking Rukwa, NNW to N-S striking northern Malawi rift faults, and the NE striking Usangu rift zone (Figures 1 and 2). Stress inversion and Kostrov summation of local and teleseismic earthquakes in the southern Tanganyika and Rukwa rifts indicate ENE extension (Lavayssière et al., 2019). Sparse geodetic data from the Tanganyika-Rukwa-Malawi rifts indicate ENE to E-W extension across the Malawi rift south of the RVP (Stamps et al., 2018). Global Navigation Satellite System (GNSS) data locally indicate NNW-SSE opening between the Tanzania craton (Victoria plate) and the eastern side of the Malawi rift, referred to as the Rovuma plate. Geodetic models of Stamps et al. (2018) predict a local stress field rotation at the Nubia-Victoria-Rovuma plate boundary (Figure 1, inset).

There are few constraints on the timing of basin initiation. U-Pb dating of detrital zircons in the post-Karroo sequences of the Rukwa rift indicates the existence of a lake basin by 8.7 Ma (Hilbert-Wolf et al., 2017). Extrapolation of modern depositional rates from drill core data to decompacted sedimentary sequences leads to an estimate of ~7 Ma (McCartney & Scholz, 2016; Scholz & Lyons, 2010), and structural and stratigraphic patterns onshore indicate that the present-day fault architecture developed after about 8 Ma (e.g., Ebinger et al., 1989; Fontijn et al., 2012).

Estimates of crustal stretching from basin modeling and fault reconstructions are <10% in the northern Malawi rift (Ebinger et al., 1991; Ellis & King, 1991). Receiver function results indicate that there is little crustal thinning beneath the RVP: crustal thickness is 38-42 km beneath the rift flanks and 39 km beneath the RVP (Borrego et al., 2018). The thinnest crust (34-38 km) occurs in areas flanking or within the Karroo rift basins (Borrego et al., 2018), suggesting that erosion of previously uplifted Karroo rift flanks and sediments has occurred. If Moho depths of ~38-42 km persist beneath the lake, it implies thinning of the crust to ~33-37 given the ~5 km of sediment (Accardo et al., 2018).

Dikes and filled cracks are oriented NNW-SSE in the Rungwe province (e.g., Ebinger et al., 1989; Fontijn et al., 2010), and faults onshore and beneath the lake strike N-S to NNW (e.g., Crossley, 1984; McCartney & Scholz, 2016; Mortimer et al., 2007). Based on seismic stratigraphic interpretations, Mortimer et al. (2007) interpret a rotation of extensional stress from ENE to NW-SE during the past 0.4 Ma. In their model, NNW striking faults are dextral strike-slip (Mortimer et al., 2007). Sparse geodetic data, however, indicate that current plate motions in the Tanganyika-Rukwa-Malawi area are ENE, with local deviations in the RVP (Stamps et al., 2018).

Time-averaged and active deformation studies lead to diverging interpretations of strain patterns. Biggs et al. (2010) suggest that active deformation along the hanging wall to the North Basin border fault indicates a temporal migration of strain from the border fault to intrabasinal faults. Seismic stratigraphic studies of time-averaged deformation in the North and Central Basin, however, indicate ongoing deformation primarily accommodated by slip on the border fault system, as well as slip along steep intrabasinal faults (Accardo et al., 2018; McCartney & Scholz, 2016). Fagereng (2013) suggests that the unusually deep crustal earthquakes in the Malawi rift occur within preexisting crustal-scale shear zones, whereas intrabasinal fault systems in strong crust have shallower seismogenic zone thickness.

3. Data

We use data from 15 broadband seismometers deployed in the RVP August 2013 to October 2015, 40 broadband seismometers deployed along the western and eastern margins of the Malawi rift between July 2014 and October 2015, 6 broadband OBS deployed between March and November 2015, and 24 short-period OBS deployed between 27 February and 21 April 2015 (Gaherty et al., 2013; Shillington et al., 2016; Figure 2). Data from two Malawi Geological Survey Reftek 120s instruments (VWZM, KARM) and the TANGA14 array of 13 stations (Hodgson et al., 2017) were also used (Figures 1, SM1). OBS had Trillium 240s and L28LB sensors. The onshore deployment included Guralp CMG3T, 40T, Streckheisen STS-2, and Trillium 40s sensors. Onshore dataloggers in Tanzania recorded at 50 sps. Malawi stations, as well as long-period OBS stations, recorded at 100 sps, and the short-period instruments recorded at 200 sps. Data for most stations are low noise (e.g., Accardo et al., 2017). P and S wave arrival times were picked manually for each event on velocity seismograms after applying a Butterworth bandpass filter between 1.5 and 15 Hz. S waves were picked on transverse components after initial locations were determined.

4. Methods

4.1. Velocity Model

We invert a subset of the SEGMeNT arrival time data to best fit a 1-D velocity model using the program VELEST (Kissling et al., 1995). VELEST simultaneously inverts for 1-D velocity structure and hypocentral parameters, providing constraints on station corrections.

4.2. Earthquake Locations

Absolute locations are determined using HYPOINVERSE-2000 (Klein et al., 2000), and the new 1-D velocity model (section 5.3 and Table SM1 in the supporting information). We also relocate six clusters of earthquakes in the RVP, North and Central basins using the double-difference location algorithm, HypoDD (Waldhauser, 2001). The algorithm uses differences in arrival times between nearby earthquakes to determine locations relative to a centroid. For example, the two ray paths between two earthquake sources and a common station are similar for events where the hypocentral separations (<10 km) are much smaller than the distance between events and stations (0-120 km; e.g., Waldhauser & Ellsworth, 2000). The residuals between observed and theoretical travel time differences are minimized for pairs of earthquakes at each station. In our implementations, the lag times of cross-correlated *P* wave onsets and absolute travel time measurements are used in the double-difference relocations.

4.3. Earthquake Magnitude and *b*-Value

Seismic attenuation in the crust is an important control on the observed amplitude of phase arrivals, and therefore, local magnitude estimates (e.g., Condori et al., 2017; Illsley-Kemp et al., 2017). Variations in attenuation, which may occur between stable lithosphere and faulted and intruded lithosphere, motivated an evaluation of the local attenuation characteristics of the Malawi rift. We estimate attenuation to develop a local magnitude scale. Local magnitudes ($\mathrm{M_L}$) for each earthquake were estimated by first convolving the seismograms with Wood-Anderson standard response to obtain displacement seismograms (Anderson & Wood, 1925) then by measuring maximum peak-to-peak amplitude on north-south and east-west horizontal components. We use both horizontal components to determine station correction terms per component, and then use the average of these values as the overall earthquake magnitude. There is no bias introduced, in comparison to standard methods of using the larger of the two horizontal amplitudes, because we have determined the N-S and E-W station corrections.

$\mathrm{M_L}$ has been defined as

$$\mathrm{M_L} = \log(A) - \log(A_0) + \mathrm{C} \tag{1}$$

where A is the observed maximum zero-to-peak amplitude of the horizontal seismogram, A_0 is the empirical distance correction, and C is an empirical station correction for each component at each station (Richter, 1935). The distance correction term using the standard 17-km normalization that enables comparison from region to region (Hutton & Boore, 1987) is

$$-\log(A_0) = n\ \log(r/17) - K\ (r-17) + 2 \tag{2}$$

where n and K are constants related to geometrical spreading and attenuation and r is the hypocentral distance of the event in kilometers. Using these new parameters, we directly solve for earthquake local magnitude and station correction terms (Keir et al., 2006; Illsley-Kemp et al., 2017; see Figure SM4 in the supporting information).

The statistical relation between earthquake frequency and magnitude provides important information on expected magnitudes. In plate boundary zones worldwide, the frequency distribution of earthquakes of any given magnitude follows a log-linear relation:

$$\log N = a - bM \tag{3}$$

where M is local earthquake magnitude and N is the number of earthquakes of magnitude larger than the magnitude threshold (Gutenberg & Richter, 1954). The largest magnitude earthquakes are rare, whereas small-magnitude earthquakes are common. The slope of the curve, *b*, is inversely proportional to the plate boundary stress (e.g., Scholz, 1968, 2015). We estimate the magnitude of completeness, $\mathrm{M_C}$, using the maximum curvature method, including the correction factor of Woessner and Wiemer (2005), and then we use the maximum likelihood method (Aki, 1965) to calculate the b-value fit of the set of earthquakes with $\mathrm{M_L} \geq \mathrm{M_C}$. The uncertainties are reported via the bootstrap method (Woessner & Wiemer, 2005), which takes into consideration the uncertainties of both $\mathrm{M_C}$ and the b-value fit.

4.4. Source Mechanisms

We estimate earthquake source mechanisms using both first motions (Snoke, 1984) and waveform modeling of two of the largest magnitude earthquakes within the array. The first-motion analyses assume a double-couple solution and use the take-off angle and backazimuth from the HYPOINVERSE solution, which includes station corrections. Given the sensitivity of take-off angles to depth, we also use waveform modeling methods to evaluate earthquake source mechanisms with depth as a free parameter.

For the two M > 4 earthquakes, full moment tensors (FMTs) are calculated using the Grond package (Heimann et al., 2018). Assuming a temporal point source, we model and fit long-period Rayleigh and Love waves (bandpass filtered to a range within 0.02-0.10 Hz). The FMT inversion, performed in the time domain, includes a built-in Monte Carlo optimization algorithm applied to objective functions perturbed using the Bayesian bootstrap method, to find a global best-fitting solution based on an L1-norm misfit function (Dahm et al., 2018; Heimann et al., 2018). In this method, we calculate the six moment tensor terms, the centroid times, and coordinates, but not source duration. The Green's functions are calculated from the 1-D velocity model from section 4.1 using the QSEIS (version 2006a) backend (Wang, 1999) of the Fomosto tool of the Pyrocko software (Heimann et al., 2017).

4.5. Stress Inversion and Kostrov Summation

Given that the earthquake cycle is much longer than the ~2-year time period of the SEGMeNT array, we compare and contrast strain rates and relative plate velocities in the northern Malawi rift using both local and teleseismically detected earthquakes (1976-2018). The approximately 40-year record of teleseismic events may be as much as an order of magnitude shorter than the seismic cycle in this slowly extending rift zone, owing to the lack of palaeoseismicity data from East Africa (e.g., Zielke et al., 2009). We take two approaches. The first is an inversion for principal stresses using a grid search algorithm (Martínez-Garzón et al., 2014). Uncertainties are quantified using the bootstrap method with 200 solutions, assuming 95% confidence limits. Only one nodal plane is used in each iteration, with the preferred nodal plane being that which is optimally oriented to a given stress state, using the approach of Vavryčuk (2014). We invert both our new focal mechanisms (63 events, Table 1) and the declustered catalogue of moment tensors from waveform modeling (18 events; Table SM2; Foster & Jackson, 1998; Yang & Chen, 2010; Biggs et al., 2010).

The second approach is the Kostrov summation, which provides the average of the individual moment tensor components weighted by their magnitudes (Kostrov, 1974). The comparison of the local and teleseismic stress inversions and the Kostrov summations and stress inversions provides some indication of the tectonic significance of the small magnitude earthquakes, which may be influenced by local, rather than tectonic stresses.

5. Results and Interpretations

5.1. 1-D Crustal Velocity Model

The earthquakes were first located with HYPOINVERSE-2000 (Klein, 2002) using a 1-D velocity model from Accardo et al. (2017). The data rarely sample the Moho so we included separate constraints: an average Moho depth of 40 km (Borrego et al., 2018) and a mantle P wave velocity of 8 km/s from a regional Pn tomography study (O'Donnell et al., 2016). Only events with at least 35 phase picks, including both *P* and *S* arrivals, where *S* wave arrivals have half the weighting factor of corresponding *P* wave arrivals, were used in the inversion. To obtain a V_p/V_s ratio representative of the selected data, we compute a Wadati diagram, which yields a best fit V_p/V_s ratio of 1.75 (Figure SM2). Applying these criteria results in 355 events used for the inversion of a 1-D *P* wave velocity model that minimizes the average (root-mean-square [RMS]) value of the travel time residuals for all events (Kissling, 1988; Table SM1 and Figure SM3). Twenty initial models were obtained by perturbing sediment and crustal velocities (Figure 3). The inversions were stopped when the velocities did not vary significantly in the subsequent inversion. The RMS residual of the initial models ranged from 1.05 to 2.10 s and decreased to 0.68 s in the final model. Further tests of the stability of the model are presented in Figure SM3. Station corrections obtained using VELEST were input to HYPOINVERSE-2000 for relocations with the new velocity model. Crustal velocities below 5 km are similar to those of the Late Proterozoic Pan-African belt in areas lacking magmatic underplate, as determined from controlled source experiments (Maguire et al., 1994; Mechie et al., 1994).

5.2. Magnitudes and *b*-Value

For the RVP and Malawi rift, we find that the geometrical spreading constant n is 0.9 and the attenuation constant K is 6.22×10^{-4}. Equation (2) becomes

$$-\log(A_0) = 0.9\ \log(r/17) - 6.22\times10^{-4}\ (r-17) + 2, \tag{4}$$

where r is distance in kilometers.

At distances less than 100 km, the attenuation in the northern Malawi rift and RVP is very similar to the Tanganyika rift (Lavayssière et al., 2019)(Fig. SM4a). The increased attenuation within the rift is consistent

Table 1
Focal Mechanism Solutions, With up to Nine Solutions and 2σ of the Strike, Dip, and Rake, Are All ≤20°

Date			Time						Focal mechanism							
Dd	mm	yyyy	Hh	mm	ss.ss	Lon (°)	Lat (°)	Depth (km)	Strike	Dip	Rake	M_L	# Sol	$2\sigma_{\text{strike}}$	# Phases	Ev #
15	7	2014	01	27	17.87	33.4438	-8.9735	13.1	269.1	42.3	-67.4	2.0	4	20	17	1
15	7	2014	21	12	05.49	33.2733	-8.8667	8.6	317.0	69.7	-52.3	2.3	1	0	14	2
21	7	2014	23	19	58.19	34.2457	-9.9602	19.9	229.4	36.2	72.9	1.9	1	0	17	3
26	7	2014	21	36	13.15	34.5133	-10.2657	25.1	182.1	42.1	-31.1	2.5	3	13	16	4
10	8	2014	19	45	08.50	33.0720	-8.7288	5.2	50.5	46.9	-69.2	3.7	1	0	44	5
12	8	2014	00	10	23.01	34.3043	-10.1633	19.2	280.2	68.5	-57.5	1.7	1	0	11	6
12	8	2014	19	48	47.36	34.2935	-10.1795	15.0	220.2	46.9	-69.2	2.4	2	5	19	7
18	8	2014	18	02	47.30	34.3725	-10.3485	17.7	29.3	41.4	-40.9	2.6	2	1	26	8
11	10	2014	23	06	49.76	34.6125	-10.1123	19.1	2.8	77.8	8.7	2.8	1	0	30	9
13	10	2014	00	50	24.88	34.4853	-11.0448	30.0	35.9	35.5	-53.9	2.3	4	12	23	10
30	10	2014	05	12	50.06	34.3813	-9.5558	25.2	6.3	81.7	-23.7	3.2	1	0	38	11
27	11	2014	22	28	25.00	34.4652	-10.9590	19.9	269.1	80.0	84.9	2.0	1	0	21	12
2	12	2014	09	15	22.31	33.7912	-9.8098	11.5	199.6	82.4	-49.5	3.1	2	9	28	13
5	12	2014	21	44	26.23	33.7915	-9.8025	12.8	25.0	85.0	-0.4	2.6	4	7	34	14
12	12	2014	02	33	31.13	34.5412	-10.3045	17.5	25.7	56.4	-71.9	2.5	3	6	29	15
15	12	2014	19	30	44.17	34.1878	-10.3025	20.0	17.4	51.6	-70.7	3.4	1	0	42	16
19	12	2014	23	07	22.75	34.2488	-10.1927	18.8	335.9	80.0	-84.9	3.8	3	10	43	17
20	12	2014	00	37	31.91	34.2560	-10.1920	17.3	333.6	31.5	-70.6	2.4	1	0	33	18
24	12	2014	19	52	39.79	33.6950	-9.1300	11.1	331.2	48.4	-62.7	2.6	2	5	34	19
31	12	2014	11	41	51.61	33.8483	-9.8482	10.8	182.0	51.6	-70.7	2.8	3	5	31	20
31	12	2014	19	47	32.87	33.8462	-9.8508	12.1	200.0	55.0	-90.0	5.2	1	0	36	21
31	12	2014	20	04	47.68	33.8518	-9.8430	9.8	251.5	60.2	-54.8	3.2	3	8	39	22
31	12	2014	20	35	11.13	33.8312	-9.8588	10.6	57.5	63.9	-24.2	3.3	1	0	37	23
1	1	2015	00	32	13.99	33.8357	-9.8245	9.1	238.3	54.4	-58.6	3.4	1	0	35	24
4	01	2015	20	02	02.40	34.5550	-10.1837	15.2	46.1	75.5	-4.0	2.2	3	2	29	25
6	01	2015	21	42	58.60	34.2833	-10.1462	19.3	167.3	65.1	-84.5	2.5	1	0	41	26
12	01	2015	22	50	07.89	33.8587	-9.8628	10.4	317.9	46.9	-69.3	2.4	1	0	37	27
18	01	2015	20	51	35.55	33.8290	-9.8650	11.3	212.1	35.3	-81.3	3.0	1	0	41	28
20	01	2015	01	07	31.26	34.0943	-9.6213	25.1	208.3	80.3	-74.8	2.9	1	0	43	29
22	01	2015	23	06	49.60	34.2860	-9.9987	23.3	335.0	40.0	-90.0	2.0	3	3	36	30
23	01	2015	23	27	33.58	33.8607	-10.0627	15.1	247.5	41.0	-74.7	2.3	2	2	36	31
28	01	2015	12	11	28.25	34.0382	-10.1375	11.2	294.1	57.4	-66.0	2.8	1	0	40	32
31	01	2015	21	09	54.46	33.8457	-9.8345	9.9	280.7	52.8	-64.6	2.1	1	0	33	33
4	02	2015	07	36	13.39	33.8128	-9.8355	11.9	355.0	45.2	-82.9	2.8	4	7	30	34
4	02	2015	22	40	42.63	34.2878	-10.0685	17.0	230.0	80.0	-90.0	1.8	1	0	25	35
16	02	2015	13	23	26.10	34.4952	-10.2162	20.0	4.9	39.7	-57.6	3.4	1	0	35	36
28	02	2015	01	45	50.98	34.3378	-10.3130	28.3	128.6	30.4	-80.1	2.0	1	0	28	37
2	03	2015	22	54	56.10	33.8383	-9.8637	11.1	298.5	55.1	-83.9	2.4	1	0	39	38
4	03	2015	00	39	17.83	33.8265	-9.8430	10.3	339.0	52.8	-64.6	2.9	1	0	50	39
6	03	2015	23	37	30.32	34.4092	-11.1775	31.5	175.0	43.9	-22.2	2.6	1	0	25	40
11	03	2015	00	19	02.71	34.3792	-11.0450	23.7	221.7	54.4	-58.7	2.2	9	16	30	41
17	03	2015	12	30	53.13	33.9463	-9.3797	14.6	320.0	55.0	-90.0	3.0	2	0	42	42
18	03	2015	21	11	34.74	33.7918	-9.9973	19.9	62.5	80.1	28.5	2.6	7	2	37	43
20	03	2015	06	40	23.03	34.1747	-9.6745	18.4	123.7	48.4	-48.1	2.6	6	5	38	44
9	04	2015	01	10	42.98	34.3933	-9.3697	30.4	176.2	84.3	34.6	4.4	1	0	50	45
2	05	2015	20	56	18.76	34.6727	-10.8868	10.0	250.0	50.0	-90.0	2.1	1	0	29	46
2	05	2015	21	32	11.23	34.6822	-10.8965	12.3	167.0	57.4	-66.0	2.0	2	1	32	47
6	05	2015	10	56	17.43	34.2917	-9.7757	30.0	184.6	46.0	-54.0	2.7	1	0	35	48
6	05	2015	22	29	57.05	34.5157	-11.2840	31.5	342.1	56.2	-53.0	2.3	1	0	26	49
9	05	2015	01	53	55.39	33.9308	-10.0457	16.0	169.7	50.1	-56.6	2.0	6	16	32	50
10	05	2015	14	42	51.31	34.1357	-10.3948	19.3	202.9	50.1	-56.6	2.7	2	2	31	51
1	06	2015	01	32	26.84	34.5862	-10.1353	12.5	352.9	60.1	-84.2	2.5	1	0	44	52
2	06	2015	21	12	01.96	34.3768	-10.5527	20.1	150.9	40.3	-82.2	2.2	3	5	31	53
5	06	2015	02	37	18.84	34.6042	-11.0928	30.2	22.5	40.3	5.9	2.6	1	0	27	54
9	06	2015	20	59	36.2	33.8600	-9.8938	27.7	197.5	80.2	-28.5	4.1	9	3	45	55
16	06	2015	17	45	16.26	34.0015	-9.2743	14.3	280.0	55.0	-90.0	3.3	3	5	45	56
17	07	2015	17	00	59.63	34.8543	-10.4147	9.3	149.3	45.9	-76.0	2.8	1	0	44	57
14	08	2015	15	15	33.07	34.4382	-10.9503	24.9	347.3	65.1	-84.5	3.3	2	10	34	58
5	09	2015	08	06	38.73	34.2470	-9.9805	25.0	184.2	50.2	-83.5	2.6	2	1	28	59

Table 1
(continued)

Date			Time						Focal mechanism							
Dd	mm	yyyy	Hh	mm	ss.ss	Lon (°)	Lat (°)	Depth (km)	Strike	Dip	Rake	M_L	# Sol	$2\sigma_{\mathrm{strike}}$	# Phases	Ev #
5	09	2015	12	18	01.07	34.2387	-9.4395	20.5	3.2	60.5	-78.5	3.4	1	0	41	60
6	09	2015	10	56	55.38	34.3313	-10.9647	22.5	184.8	45.9	-76.0	2.7	3	10	24	61
17	10	2015	06	11	07.44	34.3722	-10.0553	22.7	230.0	5.0	-0.0	3.6	1	0	23	62
18	10	2015	07	03	45.82	34.3732	-10.0628	30.5	354.2	50.2	-83.5	4.2	1	0	18	63

Note. Focal mechanisms are plotted on Figure 8. Events analyzed with waveform inversion are highlighted in bold and presented in Figure 9. All of these events are used in the stress inversion and Kostrov summation (Fig. 11).

with the presence of crustal-scale faulting and thick sedimentary and volcaniclastic sequences within the basins. However, at larger hypocentral distances where waves travel through the lower crust and upper mantle, attenuation is significantly lower and more closely resembles the Tanzanian craton (Langston et al., 1998). The new scaling provides constraints on expected ground-shaking (e.g., Midzi et al., 1999).

The local magnitude (M_L) of earthquakes detected over the 2.5-year time period of the SEGMeNT array varies between 0.67 and 5.20. We used the catalogue (1,178 earthquakes) to determine the magnitude of completeness, Mc = 1.92 ± 0.05, taking into consideration the correction factor of +0.2 as in the Maximum Curvature method of Woessner and Wiemer (2005). Using the maximum likelihood method, we estimate a *b*-value of 0.77 ± 0.03 (Figure 4).

Although the SEGMeNT array includes the RVP, the *b*-value estimate is the same (within errors) as the *b*-value of 0.75 ± 0.02 for the southern Tanganyika and northern Rukwa rifts (Lavayssière et al., 2019). The northern Malawi rift b-value is significantly less than the b-value of 0.84 for Tanzania, which includes the Archaean craton and Eastern rift (Langston et al., 1998), and b-value estimates for magmatic rift sectors in the Eastern rift: 0.87 ± 0.03 estimated for the Magadi-Natron-Manyara rift zone (Weinstein et al., 2017) and 0.87 for the central Kenya rift (Tongue et al., 1994).

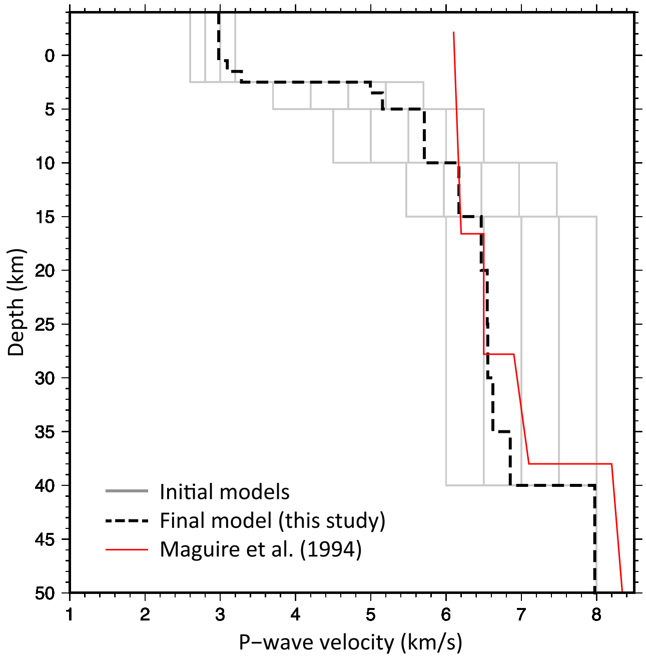

Figure 3. 1-D P wave velocity model obtained by minimizing the average (root-mean-square) value of the travel time residuals of 355 events with ≥35 phase picks. The initial models are shown as gray solid lines, and the final model is shown as a black dashed line. The red line is a crustal velocity model from controlled source experiments in the Late Proterozoic Pan-African belt, along the western margin of the Eastern Rift with minimal crustal thinning and no evidence for crustal underplate (Maguire et al., 1994). This area lacks sedimentary cover.

5.3. Earthquake Locations

5.3.1. Absolute Locations

Considering the time-varying array geometry, we included only those events within the array or at a distance from the nearest station that is ≤2 *x* hypocentral depth. This spatial filtering yields the final database of 1,178 earthquakes within the array. Of these 429 have depth uncertainties >8 km, owing to poor network geometries, particularly in the southern part of the SEGMeNT array. About 749 earthquakes have depth uncertainties less than 8 km, and with mean depth errors ≤2.8 km. Mean location errors are ≤1.5 km. Double-difference relocations improve these uncertainties, which owe in part from the short time period of OBS recordings. We outline results moving from north to south in the study region.

We were able to locate events in the Songwe basin at the northern edge of the array using some stations from the TANGA14 array (Lavayssière et al., 2019; Figure 1). As was noted in the earlier study by Camelbeeck and Iranga (1996), the Songwe basin is one of the most active parts of the region. Although the RVP was monitored for the longest time period, only 34 earthquakes at depths < 18 km occurred beneath Ngozi and Rungwe volcanoes, the two largest of the three volcanoes active in Holocene time (Figure 5). The earthquakes occurred beneath the calderas, and they occurred throughout the observation period, rather than in temporal swarms.

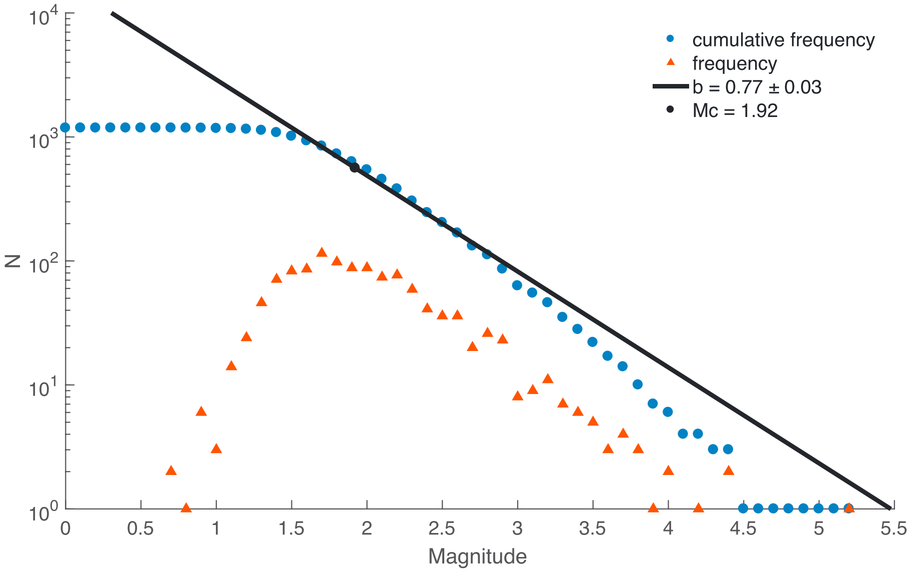

Figure 4. Using the local magnitude scaling and the adjusted maximum curvature method of Woessner and Wiemer (2005), we determine a magnitude of completeness (M_c) of M_L 1.92. The b-value estimate of 0.77 ± 0.03 was determined using the maximum likelihood method (Aki, 1965).

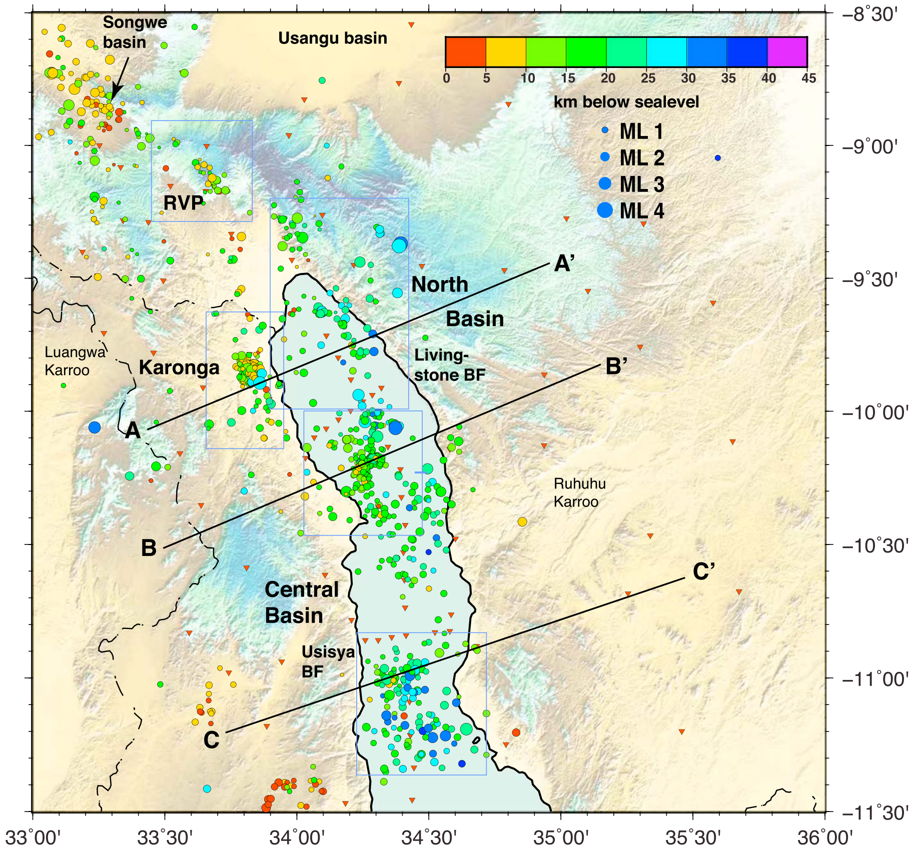

Figure 5. Absolute locations of hypocenters found using HYPOINVERSE-2000 and our new 1-D velocity model (Figure 3), color-coded with depth and scaled by magnitude. Background is hill-shade with color bar as in Figure 2. The boxes enclose areas of double-difference earthquake locations shown in Figure 6. Only a few events within the Central basin were clustered well enough to be relocated with the double-difference method, perhaps reflecting the complex faulting patterns along the Lipichili fault zone, Central Basin (LFZ in Figure 2; e.g., McCartney & Scholz, 2016).

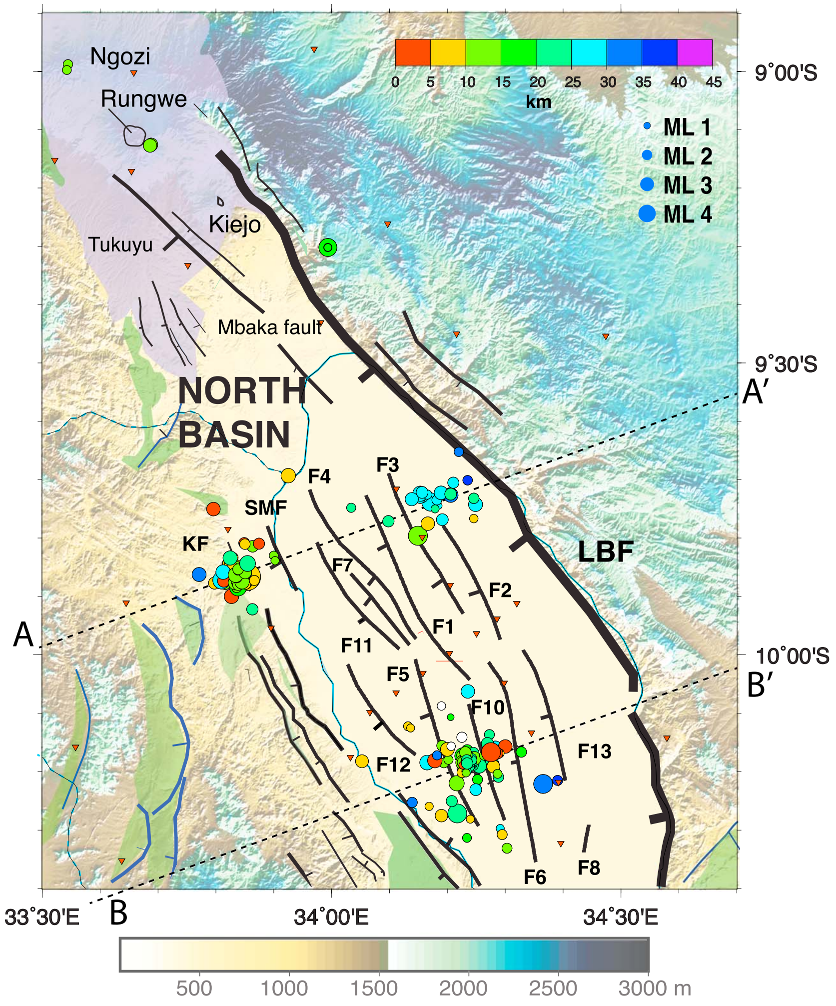

Figure 6. Double-difference earthquake locations with size scaled to magnitude and color to depth, with results combined from each of the areas shown in Figure 5. KF is Karonga fault, SMF is St. Mary fault. A-A′ and B-B′ denote central sectors of cross sections shown in Figure 8. Permo-Triassic, Jurassic, and Palaeogene strata in green; Miocene-Recent volcanic and volcaniclastic sequences in purple, as in Figure 2.

Within the North Basin, by far the most active region is the Karonga area on the western flank of the North Basin, where a Mw 5.2 (M_L 5.2, this study) earthquake occurred on 31 December 2014 (Figure 5). Over 253 aftershocks were recorded over the following 26 days, 7 of which yielded focal mechanisms (section 5.5). This same region was the site of damaging earthquakes in 2009 (Biggs et al., 2010; Kolawole et al., 2018a; Table SM2). Kolawole et al. (2018b) map sand blows and surface ruptures along the St Mary fault from the 2009 earthquakes (Figure 6). Aftershocks of the 2009 earthquakes detected by a temporary network primarily are localized along a steeply west dipping structure correlated to the St. Mary fault (Gaherty et al., 2019; Figures 5 and 6). Additional seismicity is observed on other west dipping structures beneath the lake and on an east dipping structure associated with the Karonga fault. The Karonga fault may interact with the St. Mary fault at depth (Gaherty et al., 2019; Figures 2 and 6). Further analyses of the 2014 mainshock and aftershock sequence, its comparison with deformation detected in interferometric synthetic aperture radar (InSAR), and the spatial relationship between deformation patterns with the 2009 Karonga sequence are detailed in a companion paper in preparation.

5.3.2. Relative Locations

We use the double-difference method of Waldhauser and Ellsworth (2001) to relocate earthquakes in five clusters (Figures 5 and 6). Waveform cross correlation of *P* arrivals was undertaken using a *P* wave time window size of 2.5 s, using the freeware package GISMO (Reyes & West, 2011). Assuming a 10 km nearest link distance, only 222 unique events clustered in all of the boxes combined. The weak clustering may stem from the short time period of deployment of the OBS, and the broadly distributed seismicity in space and over the ~ 30 km seismogenic thickness (Figure 4). Maximum uncertainties in depth after relocation ranged from 3.8 km in the Central basin to 0.15 km in the RVP; horizontal errors are everywhere <1.2 km. We present the double-difference results in the basin cross sections for comparison with locations of basement-involved faults.

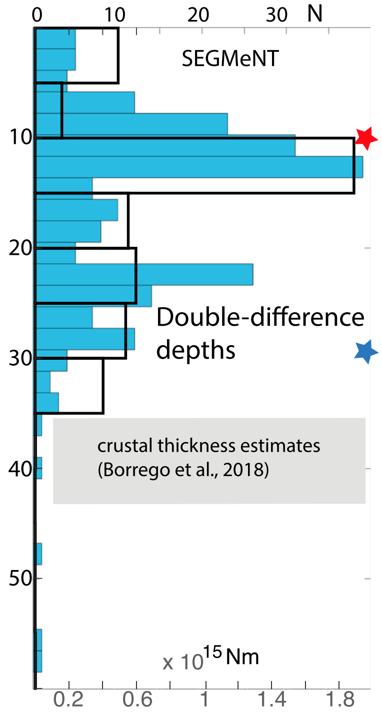

Figure 7. Histogram of hypocentral depths for the Study of Extension and maGmatism in Malawi aNd Tanzania (SEGMeNT) array from double-difference earthquake relocations in blue, overlain with black open boxes which are seismic moment release (in N-m) vs depth. The comparison shows that energy release is concentrated at depths of 10-15 km, excluding the Mw 5.2 (7.9×10^{16} Nm) earthquake in 2014 (red star indicates depth). The 9 April 2015 M_L 4.5 (7.1×10^{15} N-m) earthquake at 29-km depth (blue star) is not part of a cluster and not included in the double-difference locations. Not only do a large number of earthquakes occur in the lower crust, they represent a significant energy release.

5.4. Earthquake Depth Distribution

Many of the $M_L < 2$ earthquakes beneath the lake basin were only recorded by stations on either the western or eastern side of the lake and not by the lake-bottom stations, and this poor array geometry resulted in weakly constrained depths. Of the 1,178 events within the array, 749 had depth errors <8 km, and they show similar patterns to the double-difference relocations (Figure 6). Depths from the relocated clusters of events (222) are shown in Figure 7. There are two peaks in the depth distribution: 10-14 km and a smaller peak between 22 and 26 km. A less pronounced bimodal distribution is also seen in the depth histogram from absolute locations (Figure SM5).

We compare the depth distributions to cumulative seismic moment release by making a crude assumption that $Mw = M_L$, owing to the few calibrated earthquakes with which to make comparisons: the 2014 Mw 5.2 (M_L 5.2) and mb 4.25 (M_L 4.5) events at 10 and 29 km, respectively, recorded during the SEGMeNT deployment (Table 1). For earthquakes of mb ≤ 5, mb is approximately the same as Mw (Gasperini et al., 2013). The pattern of moment release vs depth will not change with a better-constrained scaling relation, but the absolute values of course will. We then assume that $Mw = (\log M_0 - 9.1)/1.5$ with M_0 in N-m (*IASPEI*, 2013). Note that the 9 April 2015 M_L 4.5 earthquake at 29-km depth beneath the eastern rift flank was not part of a spatial cluster, so not in the double-difference catalogue. The 31 December 2014 Mw 5.2 earthquake at 10-km depth ($M_0 = 7.9 \times 10^{16}$) is more than 10 times larger than the summations of the other earthquakes and is omitted. We omit that earthquake to better illustrate the pattern of microseismicity (Figure 7). The peak in energy release matches the maximum frequency of earthquake depths, but there remains significant energy release by lower crustal earthquakes, particularly when considering the Mw4.5 event at 29 km (7.1×10^{15} N-m).

5.5. Earthquake Source Mechanisms

Earthquakes with clear *P* arrivals on 11 or more stations and with azimuthal gaps ≤120° were screened for focal mechanism solutions. Examples of normal and strike-slip earthquake focal mechanism are shown in Figure SM6. Of the ~200 earthquakes considered, 63 had strike, dip, and rake of the better-constrained slip plane each with $2\sigma \leq 20°$ (Table 1). Considering the lateral variations in shallow crustal structure that adds uncertainty to take-off angles, we allowed one *P* phase error if within 5° of a nodal plane (e.g., Figure SM6).

First motion focal mechanism solutions for earthquakes in the crust show a full range from normal dip-slip to strike-slip (9, 11, 23, 25, 43, 45, and 55), and even reverse faulting (3; Figure 8). Most of the normal faulting mechanisms have two steep (~ 45°) nodal planes (e.g., 1, 5, 7-8, and 15-16; Figure 8).

The two largest earthquakes recorded by the SEGMeNT array are a M_L 5.2 in the Karonga region on 31 December 2014 (Event 21) and a M_L 4.5 on the uplifted footwall block of the Livingstone border fault on 9 April 2015 (Event 45; Figure 9). No local network was in place to locate the 2009 earthquakes with comparable accuracy, but InSAR and aftershock studies provide fairly tight constraints on the fault geometry (Biggs et al., 2009; Gaherty et al., 2019). The FMT obtained for Event 21 using 25 stations has a nearly N-S strike and is located to the north of the series of nine M ≥ 4.9 main shocks within two weeks in December 2009 (Biggs

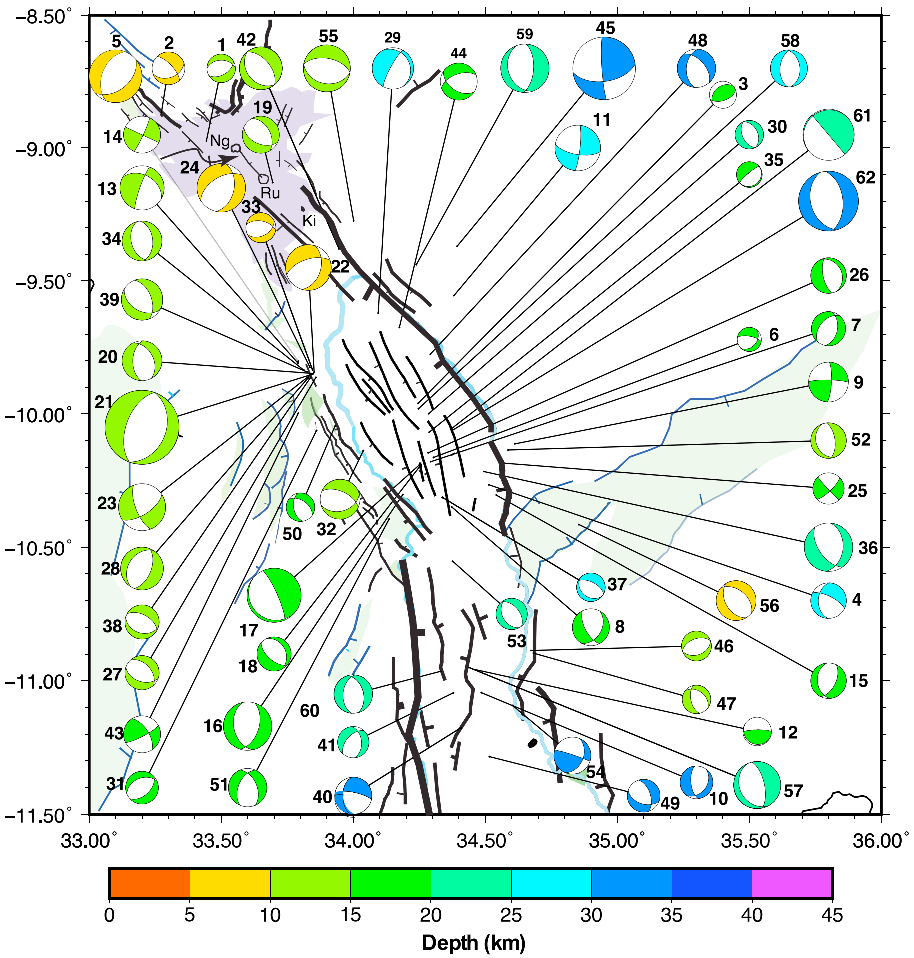

Figure 8. Compilation of 63 first motion focal mechanisms determined from the Study of Extension and maGmatism in Malawi aNd Tanzania (SEGMeNT) array and permanent stations in Malawi, color-coded with focal depth. Numbers correspond to the event numbers in Table 1. Events 21 and 45 were also analyzed using FMT inversion (Figure 9). As in Figure 2, Miocene-Recent faults in black; Permo-Triassic, Jurassic faults in dark blue; green infill indicates Permo-Triassic, Jurassic sedimentary units; purple denotes Miocene-Recent lavas and volcaniclastics of the RVP. Ng = Ngozi volcano; Ru = Rungwe volcano; Ki = Kiejo volcano.

et al., 2009; Gaherty et al., 2019). On the other hand, the FMT of Event 45 obtained using 23 stations is a strike-slip mechanism. The centroid depths are both within 2 km of the catalog depth, indicating robust catalog depths. In addition, the double-differenced relocated depth of Event 21 is the same as the centroid depth. This suggests that Event 45 is definitively in the lower crust, as estimated independently using moment tensor inversion.

Both events have similar FMTs and first-motion focal mechanisms, but with slight nodal plane rotations. Note that the first-motion method is most sensitive to the initial rupture, whereas the moment tensor reflects the averaged rupture. The nodal plane discrepancy could be attributed to uncertainty in focal mechanism determination or may reflect a real difference in source processes. For example, a curved fault rupture will show an initial rupture mechanism that is different to an averaged rupture mechanism (e.g., Frohlich, 1994; Hicks & Rietbrock, 2015).

Event 21 also appears on the global centroid moment tensor catalog (gCMT; Ekström et al., 2012), with a similar N-S trending strike as our FMT, and at a depth of 12 km, as in our local catalog. Assuming a moment tensor decomposition to isotropic + double-couple + compensated linear vector dipole, the gCMT for Event 21 is 98% double-couple, whereas the calculated FMT has only 37% double-couple. The source-type discrepancy between the deviatoric global CMT and our FMT might indicate regional MTs capturing non-

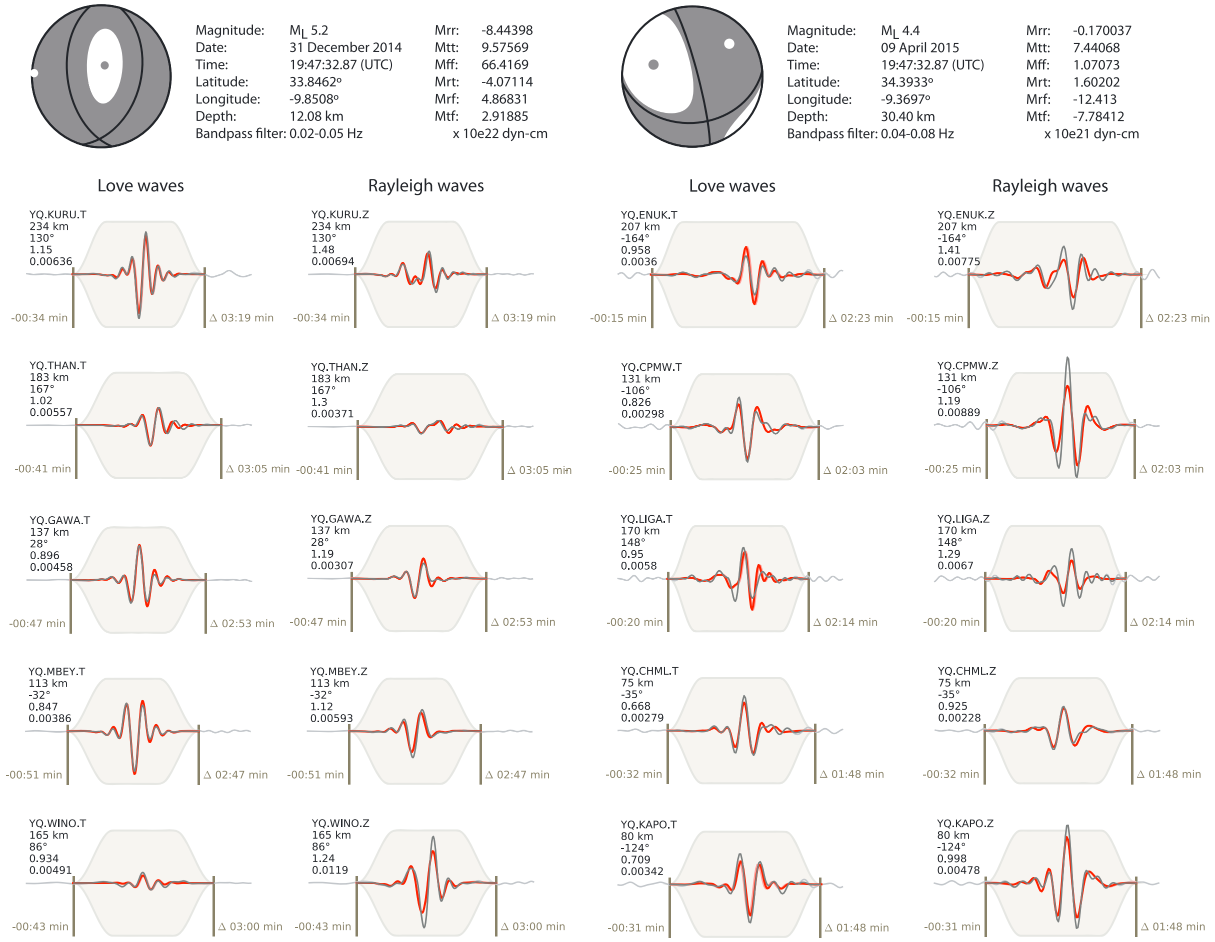

Figure 9. Full moment tensor solutions (velocity seismograms) obtained using Grond (Heimann et al., 2018) for the two largest events recorded by the Study of Extension and maGmatism in Malawi aNd Tanzania (SEGMeNT) array. P and T axes shown as black and white circles, respectively. Five sample synthetic waveform fits (red) plotted on top of data (black) are shown for each event. Light gray traces are untapered data waveforms, and light red traces are unshifted synthetic waveforms. The information on the top left of each waveform includes the station name, station-to-receiver distance, azimuth, weighting factor, and relative residuals.

double-couple processes better than global MTs (e.g., Oliva et al., 2019), a topic being explored in more detail through comparisons with models of InSAR data. The Karonga region is 50 km south of the RVP, but far enough away and without evidence of crustal modification (e.g., Borrego et al., 2018), so it is unlikely that Event 21 is magma-related. Magmatism likewise was ruled out in geodetic and seismic studies of the 2009 Karonga sequence (Biggs et al., 2010; Gaherty et al., 2019). Comparison of local and gCMT source mechanisms of main shock, and aftershocks with InSAR is underway, and will be reported separately. The non-double-couple source component may be attributed to hydrothermal fluids interacting with the fault or a complex rupture geometry such as a curved fault.

5.6. Rift Kinematics

Only 11 of the 63 earthquakes with focal mechanisms are in or along the flanks of the Central Basin, too few to obtain robust results using the stress inversion algorithm, and precluding evaluation of along-axis variations between the Songwe basin, RVP, North and Central basins (Figure 10).

5.6.1. Local Earthquakes

The Martínez-Garzón et al. (2014) implementation of the Hardebeck and Michael (2006) stress inversion estimates uncertainties in principal stresses and stress ratio, R, using the random bootstrap resampling of the input fault planes. We have removed focal mechanisms for the foreshock and aftershocks of the 31 December 2014 Mw 5.2 earthquakes to create a declustered data set (N= 58). This declustering is done to

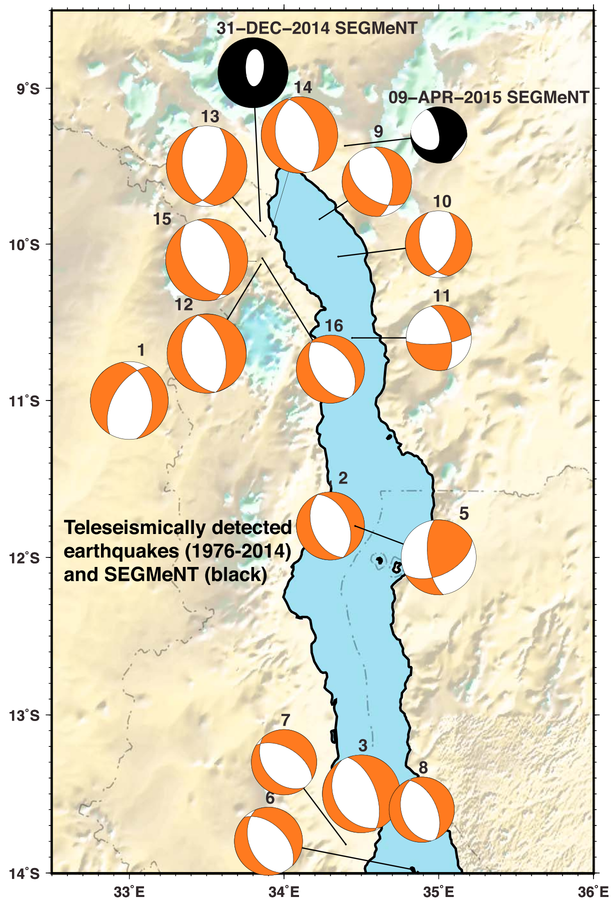

Figure 10. Source mechanisms from waveform modeling for earthquakes detected teleseismically (M > 4.5; orange) from Yang and Chen (2010), Jackson and Blenkinsop (1993), Foster and Jackson (1998), Dziewonski et al. (1991), Ekström et al. (2012), Biggs et al. (2010), and our new full moment tensor solutions for the M_L5.2 and M_L4.5 earthquakes recorded by the SEGMeNT array (Figure 9, Table SM2). Location errors of the teleseismically detected earthquakes may be 30 km or more.

satisfy the assumption of stress homogeneity within the study area, as aftershocks may accommodate local stresses induced by the main shock. The local earthquake inversion shows sub NE-SW directed extension (N58° +28/-10) and nearly vertical σ_1 (Figure 11a).

The Kostrov summation of local earthquakes shows a WNW-ESE opening direction (*T* axis of 286°E; Figure 11b). The Kostrov summation is dominated by the 2014 M_L 5.2 Karonga earthquake mechanism, which differs in strike by 20° from the waveform inversion, explaining the difference between the two extension directions (Figure 11b). Owing to the non-double component determined in the FMT inversion, we prefer the ENE-WSW direction (Figure 11a) from stress inversion results.

5.6.2. Teleseismically Detected Earthquakes

Earthquake source mechanisms determined from waveform modeling in studies by Dziewonski et al. (1981), Jackson and Blenkinsop (1993), Foster and Jackson (1998), Biggs et al. (2010), Yang and Chen (2010), Ekstrom et al. (2012), and this study (Figure 9) form the basis for parallel analyses (Figure 10 and Table SM2). Owing to the small number and much larger location uncertainties of teleseismically detected earthquakes (~10-30 km), we also include earthquakes from the southern basin of the Malawi rift. The teleseismically detected earthquakes include the 2-week 2009 swarm that initiated with a M5.2 earthquake, with the two largest earthquakes (M5.5 and M6.0) occurring later in the swarm (Biggs et al., 2010). We treat all but the M5.5 and M6.0 events as aftershocks and remove them from the stress inversion data base.

The σ_3 direction from the stress inversion of Malawi rift teleseismically detected earthquakes is N64° +/-20°, and R = 0.32 (Figure 11c). The Kostrov summation for the same 40-year teleseismic record provides a T axis

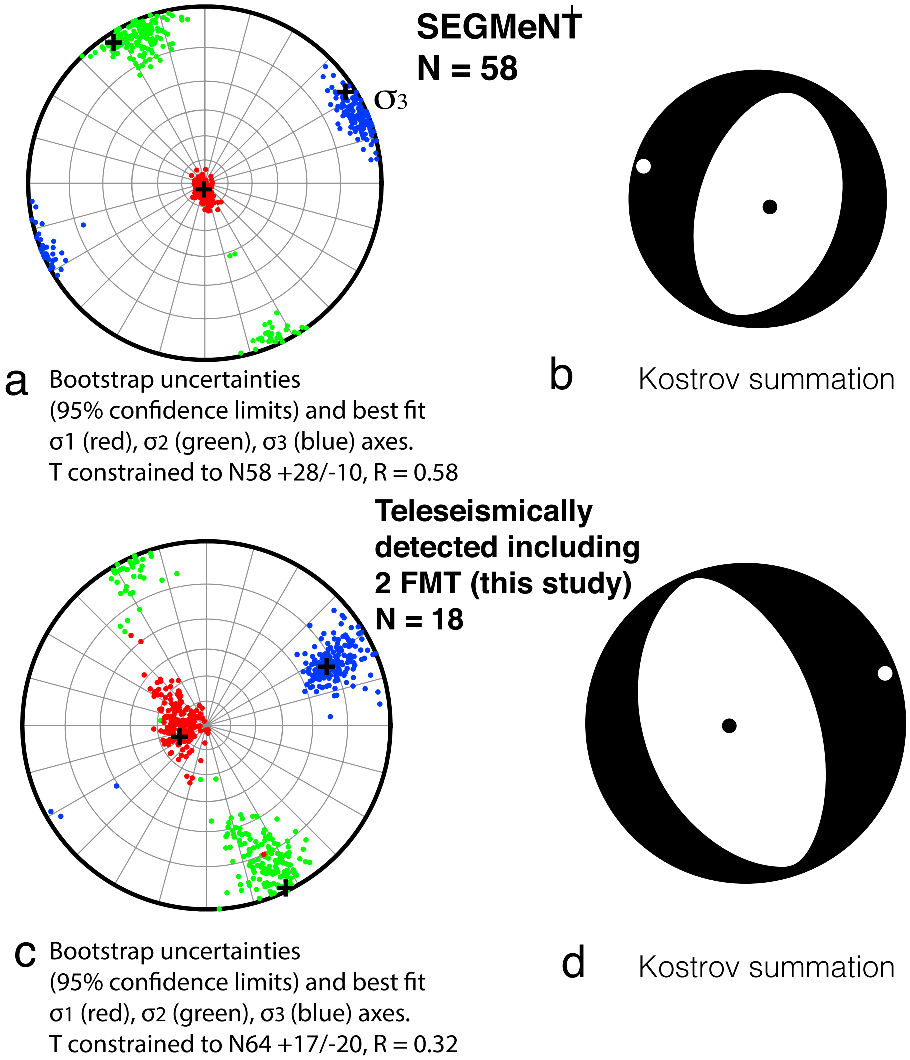

Figure 11. Comparison of grid search stress inversion using the MSATSI program (Martinez-Garzon et al., 2014) and Kostrov summation results for (a and b) local and (c and d) teleseismic earthquakes where inputs are weighted by magnitude. (a) Bootstrap uncertainties with 95% confidence limits about best-fitting σ_1, σ_2, σ_3 indicated by crosses, using the focal mechanisms in Table 1. (b) Kostrov summation of earthquakes in Table 1 and Figure 8. (c) Bootstrap uncertainties with 95% confidence limits about best-fitting σ_1, σ_2, σ_3 indicated by crosses, using the focal mechanisms in Figure 10 and Table SM2. (d) Kostrov summation of earthquakes in Table SM2. The teleseismic inversion indicates an approximately N70°E rift extension direction that is consistent with the stress inversion. The exception is the Kostrov summation of the local earthquakes that is strongly influenced by the two largest earthquakes. The similarity between local and teleseismic stress inversion indicates that the local earthquakes are representative of tectonic stress.

(σ_3) of N70°E and an extensional strain rate of 1×10^{-17} s^{-1} or 4×10^{-10} $year^{-1}$ (Figure 11d). The calculated seismic strain rate is about 25 times smaller than the average geodetic strain rate in approximately the same area (Stamps et al., 2018). The discrepancy between the seismic and geodetic strain estimates is intermediate between that of a magmatic rift (e.g., Northern Tanzania Divergence, Weinstein et al., 2017) and a magma-poor rift (e.g., Southern Tanganyika rift; Lavayssière et al., 2019). Part of the seismic strain deficit may be due to aseismic deformation within the RVP, which has experienced only minor earthquake activity during the time period of the SEGMeNT array, and instrumental records (Figure 11d). The low *b*-value indicates strong coupling across crustal-scale faults, allowing for the possibility of rare M > 7.5 earthquakes not captured in the historical and instrumental earthquake catalogues.

The Kostrov and stress inversion results for the teleseismically-detected earthquakes (Figures 11c and 11d) are nearly identical and are very similar to the local earthquake extension direction estimates (Figure 11a).

The similarity between results weighted by magnitude (Kostrov summation), inversion of local earthquakes, and teleseismic earthquakes indicates that the ensemble of earthquakes recorded on the temporary array is representative of tectonic processes.

5.7. Basin Profiles

We use rift perpendicular profiles to illustrate the 3-D structure of the North and Central basin and the geometry of border faults at depth within the crust, with particular focus on fault slip kinematics (Figure 12). The cross sections are made parallel to extension direction estimated from stress inversion of earthquake source mechanisms (Figure 11d). For the purposes of these cross sections, the dip of the border faults is assumed to be constant and 50°-60°. Along all cross sections, variation in Moho depth beneath basins is assumed to be minor (Borrego et al., 2018).

Profiles A-A′ and B-B′ cross the central and southern parts of the North Basin, respectively, which is an ~70-km-wide, eastward tilted half-graben. The western side of the basin is a faulted monocline that exposes eroded and tilted Karroo and Cretaceous sedimentary strata (Figures 2, 8, and 12). Basement-involved faults imaged in reflection data beneath the basin are synthetic to the Livingstone border fault; the eastward tilted Karonga fault exposed onshore is the exception (e.g., Scholz, 1989 Gaherty et al., 2019). Profiles were chosen to pass through the most intense clusters of earthquakes detected by the SEGMeNT array and to follow seismic reflection profiles, allowing comparison of shallow and deep fault systems, and short-term and time-averaged deformation patterns (Figures 2 and 5). Profile A-A′ transects the 31 December 2014 mainshock-aftershock sequence, which ruptured at the intersection of the conjugate St. Mary and Karonga faults. The preferred nodal plane for the mainshock is the westward tilted plane (St. Mary fault), but aftershocks appear to correspond to slip on both faults. Focal mechanisms are steep and occur along projections of the westward-dipping St Mary fault (Figures 6 and 12). Earthquakes occur along the projection of the border fault and intrabasinal faults to depths of 30-40 km.

Profile B-B′ shows a similar basin form as A-A′. As along A-A′, basement-involved faults are synthetic to the Livingstone border fault. Notable is the apparent absence of faulting on the western rift flank; instead, seismicity is focused along Faults 10 and 6 (Figure 6). Fault 6 (F6; Figures 6, 8, and 12) is an intrabasinal fault with more than 1.5 km of vertical displacement. Seismicity along intrabasinal faults occurs from the base of 1- to 5-km-thick sedimentary packages to 35 km below sea level. Nodal planes match the projections of steep normal faults to the lower crust and argue against listric fault geometries at least at depths shallower than 25 km.

Profile C-C′ crosses the eastward tilted Central Basin, whose eastern margin is cut by a large offset fault. Based on seismic reflection imaging, the center of the basin is a narrow horst, referred to as the Lipichili fault zone (LFZ; McCartney & Scholz, 2016; Figures 2 and 12). Lower crustal seismicity to depths of 30 km occurs along projections of both the Usisya border fault, and the eastern fault system, as well as beneath the LFZ. Focal mechanisms also indicate slip along steep nodal planes corresponding to border and intrabasinal faults.

6. Discussion

The new constraints on the depth of the Moho (Borrego et al., 2018) allow us to evaluate the geometry, kinematics, and depth extent of border faults, to reconsider depth distributions interpreted from limited teleseismic earthquakes, and to place the persistent Mw > 6 lower crustal earthquakes, typical of the Western rift system, in tectonic context.

6.1. Distribution of Active Faulting

The North and Central basin profiles demonstrate broad, half-graben basins whose large-basin and flank dimensions indicate deformation of strong, thick lithosphere (e.g., Ebinger et al., 1991; Weissel & Karner, 1989). Based on the time-integrated deformation and stratigraphic patterns, strain is localized to the Livingstone and Usisya border fault systems (e.g., Accardo et al., 2018; Ebinger et al., 1991; McCartney & Scholz, 2016).

In their analyses of ground deformation associated with the 2009 earthquake sequence, Biggs et al. (2010) suggest that crustal deformation has migrated from the border faults to intrabasinal faults. Comparison of

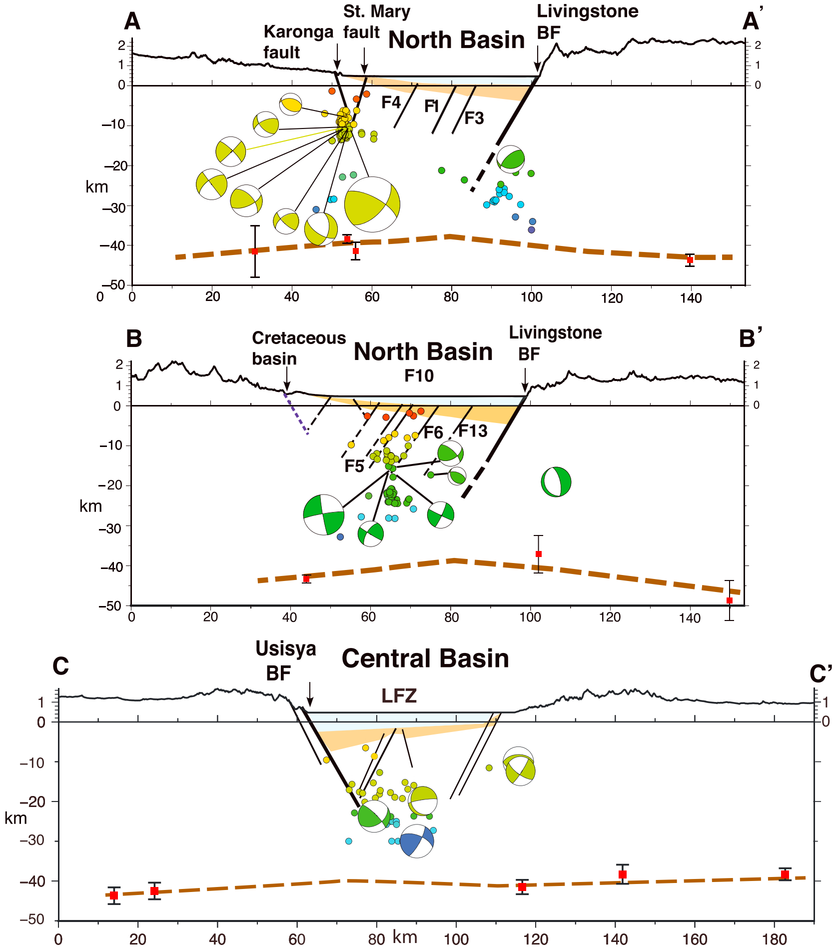

Figure 12. (a–c) Cross-rift Profiles A-A′, B-B′ across the North Basin, and C-C′ across the Central Basin (Figures 5 and 6). Double-difference earthquake locations are shown along Profiles A-A′ and B-B′, and absolute locations are shown on C-C′. Focal mechanisms within ± 5 km of each profile are projected into the line of the cross sections. The red squares mark Moho depth estimates within ±10 km of the line of the cross-section with their associated error bar from receiver functions (Borrego et al., 2018). The dashed brown line provides an approximate Moho geometry. St. Mary and Karonga faults from Kolawole et al. (2018b), Biggs et al. (2010), and Gaherty et al. (2019). Numbered faults in Figure 6. Along C-C′, LFZ is Lipichili fault zone after McCartney and Scholz (2012).

seismicity along Profiles A-A′ and B-B′ illustrates significant along-strike variations in the distribution of earthquakes, which is expected considering that our experiment has captured an instant in the much longer earthquake cycle of many active faults. Our analyses of well-located seismicity during the 2.5-year SEGMeNT monitoring period indicate that both border and intrabasinal faults are actively accommodating extensional strain across the basin. Specifically, seismicity is located along segments of the Livingstone and Usisya border faults, and it occurs at midcrustal to lower crustal depths (e.g., Figures 6 and 12). Earthquake patterns indicate that steep, deep border faults remain active through at least 8 Myr of basin history and that intrabasinal faults may also penetrate to the lower crust. Similar patterns are seen in the southern Tanganyika rift, where the most energetic, lower crustal earthquakes occur along projections of border faults (Lavayssière et al., 2019).

River drainage, lake bathymetry, and stratigraphic patterns all indicate modern tilting along the Livingstone and Usisya border faults, consistent with observations of ongoing border fault slip (e.g., Ebinger et al., 1993; McCartney & Scholz, 2016; Accardo et al., 2018). Offsets on a prominent 75-kyr-old horizon by intrarift faults in the North basin indicate that intrarift faults, including F6, have likely been active in the Holocene (Figures 6 and 12).

Several clusters of seismicity correspond to the expected intersection of conjugate faults, based on projections of shallow fault dips to subsurface. Examples are the intersections of the St. Mary and Karonga faults at ~10-km depth along Profile A-A′, and the intersection of the Usisya and Lipichili faults at ~20-km depth along Profile C-C′ (Figure 12). Aftershocks of the 2009 earthquake sequence in the Karonga region also cluster at the inferred intersection of the conjugate St. Mary and Karonga faults, but along a greater length of the two faults than those of the 2014 earthquake and aftershocks (Gaherty et al., 2019). Similar patterns are seen in the Tanganyika rift where earthquakes also cluster at the inferred intersection of conjugate border faults at depths of 25-35 km (Lavayssière et al., 2019).

6.2. Extension Direction

Extension direction in the southern Rukwa and northern Malawi rift zones has been debated for three decades, in part owing to data gaps in this formerly remote region. Tiercelin et al. (1988) and Chorowicz (2005) apply mid-ocean ridge-transform kinematics to interpret the Rukwa rift and North basin of the Malawi rift as a right-lateral transform linking the NW-SE opening Tanganyika and Malawi rifts. Owing to the finite width of the deforming rift zones, both sinistral and dextral motions are expected where 80- to 120-km-long border faults are linked by relay ramps and oblique-slip faults that interact in space and time (e.g., Ebinger et al., 1989; Morley et al., 1990). Delvaux et al. (2001) and Chorowicz (2005) interpret NW-SE strike-slip faults linking the North and Central basin, but the basis for this interpretation is unclear. Ebinger et al. (1989) considered the orientation of dikes and aligned cinder cones to interpret an ENE extension direction. Delvaux (2001), Ring et al. (1992), and Mortimer et al. (2007) use palaeostress measurements onshore and fault orientations beneath the lake to interpret a rotation of the stress field from ENE to ESE in Quaternary time. Based on stress inversion of local earthquake focal mechanisms and a smaller catalog of source mechanisms of teleseisms from the Malawi rift and south to -17°, Delvaux and Barth (2010) determine a N62°E opening direction that matches our stress inversion and Kostrov results using a longer time series. These interpretations assume that fault orientation is optimally oriented to the assumed stress field.

Earthquake data are inadequate to evaluate a possible local stress field rotation in the narrow Songwe basin between the Rukwa and Malawi rift. Only four earthquakes with focal mechanisms are located in the Songwe basin (1, 2, 5, and 14), where ENE and NW-SE extension has been interpreted from waveform modeling of four additional earthquakes detected on temporary arrays (Ferdinand et al., 2002; Brazier et al., 2005; Delvaux & Barth, 2010).

Our results do not support the interpretations of modern, NW-SE extension direction in the RVP and northern Malawi rift. Instead, the stress inversion and Kostrov summation analyses of local and teleseismic earthquakes indicate an extension direction of about N65°E, consistent with the range of opening directions from continuous GNSS data north and south of the RVP (Stamps et al., 2018). Although individual focal mechanisms of earthquakes with $M_L < 3$ show a range of orientations, some may not be tectonic. These smaller magnitude earthquakes represent a trivial amount of seismic energy release (e.g., Figure 7). The orientation of border and intrabasinal faults and the active seismicity suggest that extension direction has remained roughly ENE-WSW over the past ca. 8 My, or perhaps longer.

Sparse and temporally variable Global Positioning System (GPS) velocity data from the RVP and Usangu rift at the northern boundary of the Rovuma microplate indicate a rotation from ENE to SE opening direction (Saria et al., 2014; Stamps et al., 2018). Focal mechanisms for three earthquakes 1 (M_L 2.0), 44 (M_L 2.6), and 56 (M_L 3.3) suggest sub-N-S opening between the presumably rigid Tanzania craton and Rovuma plate as predicted in the Stamps et al. (2018) model. Yet, the majority of earthquakes in this zone (11, 19, 29, 42, 45, and 60) argue against the local stress field rotation to NW-SE in the Usangu and RVP area interpreted from GPS data (Stamps et al., 2018). The approximately 100-year-long historic seismic catalogue may miss a large magnitude sub-N-S opening event between the Tanzania craton (Victoria plate) and Rovuma microplate. Alternatively, the local NNW-SSE opening from GPS sites in the RVP may capture along-axis hinging: uplift in the Rungwe province relative to the subsiding, spoon-shaped North Basin. The bending may be in response to surface and intrusive loads or to more local volcanic and hydrological pressure fluctuations at Rungwe, Ngozi, and Kiejo volcanoes, as seen in other parts of the rift (e.g., Weinstein et al., 2017; Wood et al., 2017). Stamps et al. (2018) omitted data from the Virunga volcanic province in the northern sector of the Western rift owing to along-axis tilting, but a similar process may affect GNSS results here.

6.3. Lower Crustal Earthquakes

Seismogenic thickness across both the North and Central rift basins is approximately 30 km, with no clear difference across and along-strike (Figures 5 and 12). The unusually thick seismogenic layer is complementary to estimates of unusually high plate strength in the Malawi rift area, with effective elastic thickness (Te) of 20-30 km from forward and inverse models of gravity and topography (Ebinger et al., 1991; Pérez-Gussinyé et al., 2009). Crustal Poisson's ratio estimates of 0.23-0.26 from receiver function analyses of basins south of the RVP suggest a felsic to intermediate bulk crustal composition (Borrego et al., 2018), although these values also overlap the range for amphibolite gneiss and some granulites at lower crustal pressures of 200-300 MPa (0.24-0.27; Christensen, 1996; Wang & Ji, 2009). Hellebrekers et al. (2019) examined failure of mafic gneisses from the Malawi rift and observed little or no change in frictional properties or microstructures to lower crustal pressures of 300 MPa and temperatures of 700°C expected in the Malawi rift lower crust. Failure occurred by cataclasis, consistent with a high viscous strength of mafic materials (Hellebrekers et al., 2019). Considering the lack of evidence for magma intrusion south of the surface expression of the RVP, our preferred interpretation of lower crustal seismicity beneath the Malawi rift flanks and basin is a strong mafic gneiss and granulite lower crustal composition.

6.4. Hazard Implications

The long, contiguous border faults, lower crustal seismicity, and strong lithosphere have both intrigued and sobered research scientists: Do ~100-km-long, structurally contiguous border faults rupture in M7.5-8 earthquakes (Hodge et al., 2015; Jackson & Blenkinsop, 1993; Yang & Chen, 2008)? Although there are no palaeoseismicity studies in the Western rift, the combined SEGMeNT and TANGA14 (Lavayssière et al., 2019) seismicity studies provide new insights into plate coupling in cratonic rift zones.

The largest historic earthquake, M7.4, in East Africa occurred in 1910 in the Rukwa rift between the Tanganyika and Malawi rifts (Ambraseys, 1991). Although attenuation is high locally within the faulted rift basins, seismic energy from lower crustal earthquakes is transmitted efficiently through cratonic lithosphere, indicating that moderate to large earthquakes will be felt regionally (Figure SM4). The b-values and depth distribution of moment release in the northern Malawi and southern Tanganyika rifts are similar and indicate strong coupling between hanging wall and footwall of the border fault systems. In both areas, b-value is less than 0.8, and seismogenic layer thicknesses are 30 and 40 km, respectively. Similar b-values and depth distribution of energy release occur in subduction zone settings where megathrust fault systems also span the entire crustal thickness (e.g., Bilek & Lay, 2018; Tormann et al., 2015). Our results indicate a factor of 25 or greater deficit in seismic energy release as compared to comparable geodetic moment release over the past 40 years. Combined with the low *b*-value indicating strong plate coupling, we suggest that $M > 7.5$ earthquakes associated with rupture of entire border faults do occur, but with repeat times too long to be captured in the historical record (<120 years for much of the Western rift).

Prior to our local seismicity study, only teleseismically detected earthquakes ($M > \sim 4.5$) with location errors of 10-30 km were available, and crustal thickness estimates were lacking. Based on teleseismic earthquake and structural patterns, Fagereng (2013) suggests that lower crustal seismicity is localized along border faults that exploit pre-existing weak zones. In his model, intrabasinal faults form in strong crust with shallow seismogenic layer thickness (Fagereng, 2013). Our work shows that seismogenic layer thickness is 25-35 km across the uplifted flanks and basins, arguing against the weak border fault zone hypothesis (e.g., Figure 12). Local seismicity studies with small location errors show that lower crustal earthquakes also occur along intrabasinal and border faults in the Tanganyika and Rwenzori sectors of the Western rift (Lindenfeld et al., 2010; Lavayssière et al., 2019), providing context for the teleseismically detected earthquakes (e.g., Craig et al., 2011; Yang & Chen, 2010). The *b*-values significantly less than 1 indicate strong coupling in all of these settings. The clear differences between the intrabasinal and border faults are their lengths: intrabasinal faults are 20-40 km long, whereas the border faults are more than 100 km in length (e.g., Accardo et al., 2018; Ebinger et al., 1991). A characteristic 30-km intrabasinal fault length is consistent with a Mw 6.5 earthquake rupture, if we assume a slip of 1 m, a shear strength of 32 GPa, and seismogenic layer thickness of 30-40 km. Similar patterns are observed in the S. Tanganyika rift where several Mw > 6 earthquakes have been located (Lavayssière et al., 2019; Yang & Chen, 2010).

7. Conclusions

We use the 2013-2015 onshore-offshore SEGMeNT seismic array and permanent Malawi stations to analyze the time-space patterns of seismic deformation in the southern Rukwa rift, RVP, and northern Malawi rift. Earthquakes are relocated using a new regional 1-D velocity model, and clusters are analyzed using double-difference methods. Using the new magnitude scaling relation and station correction terms, magnitudes of the 1,178 earthquakes within the SEGMeNT array are $0.7 < M_L < 5.2$ with a b-value 0.77 ± 0.03, and magnitude of completeness M_L 1.9. Although the SEGMeNT array includes the RVP, the b-value estimate is the same (within errors) as the b-value of 0.75 ± 0.02 for the southern Tanganyika and northern Rukwa rifts. The low b-value indicates strong coupling across border and intrabasinal faults. Although teleseismically detected earthquakes between 2009 and 2014 have had focal depths < 15 km, the seismogenic layer is 30-35 km in both the North and Central basins, with little difference between ~100- and 120-km-long border faults and ≤30 km-long intrabasinal normal faults. Focal mechanism solutions for 63 earthquakes reveal predominantly normal and oblique-slip motion with steep nodal planes. Along representative rift profiles, steep nodal planes correspond to projections of surface faults to lower crustal depths. The earthquake patterns in the Malawi rift indicate frictional failure in strong crust, arguing against significant heating outside the RVP.

The stress inversion and Kostrov summation analyses of local and teleseismic earthquakes indicate a modern extension direction of about N65°E, with little indication of a local rotation in the RVP or Usangu area. Earthquake patterns, therefore, indicate that steep, deep border faults remain active through at least 8 Myr of basin history. Seismic strain rate estimated from Kostrov summation of Malawi rift teleseisms is about 25 times smaller than strain rates from models of sparse geodetic data, implying that time scale of monitoring is too short to sample the largest magnitude earthquakes and that some rift opening is accommodated aseismically. The low b-value, border fault lengths >100 km, and evidence for aseismic deformation within the Tanganyika-Rukwa-Malawi zone together indicate that infrequent $M > 7.5$ earthquakes are possible within this cratonic rift.

Acknowledgments
We thank Olaf Zielke and an anonymous reviewer for constructive comments on the manuscript. We are grateful for the assistance of many during the siting and acquisition of the passive earthquake monitoring, with special thanks to Gabriel Mbogoni, Marsella Kachingwe, Godson Kamihanda, Gabrielle Tepp, John Paul O'Donnell. Shelby Corning helped build the earthquake catalogue. C. E. acknowledges support of National Science Foundation grant 1734884. F. I. K. is funded through the New Zealand Ministry of Business, Innovation, and Employment funded ECLIPSE program. All seismic waveform data are archived at IRIS (SEGMeNT doi:10.7914/SN/YQ_2013), and the earthquake catalogue has been provided to the International Seismological Centre for open access. The absolute earthquake catalogue is also available for download with the supporting information.

References

Accardo, N. J., Gaherty, J. B., Shillington, D. J., Ebinger, C. J., Nyblade, A. A., Mbogoni, G. J., et al. (2017). Surface wave imaging of the weakly extended Malawi Rift from ambient-noise and teleseismic Rayleigh waves from onshore and lake-bottom seismometers. *Geophysical Journal International*, *209*(3), 1892–1905. https://doi.org/10.1093/gji/ggx133

Accardo, N. J., Shillington, D. J., Gaherty, J. B., Scholz, C. A., Nyblade, A. A., Chindandali, P. R. N., et al. (2018). Constraints on rift basin structure and border fault growth in the northern Malawi rift from 3-D seismic refraction imaging. *Journal of Geophysical Research: Solid Earth*, *123*(11), 10–003. https://doi.org/10.1029/2018JB016504

Aki, K. (1965). Maximum likelihood estimate of b in the formula log $N= a\text{-}bM$ and its confidence limits. *Bulletin of the Earthquake Research Institute-University of Tokyo*, *43*, 237–239.

Ambraseys, N. N. (1991). The Rukwa earthquake of 13 December 1910 in East Africa. *Terra Nova*, *3*(2), 202–211. https://doi.org/10.1111/j.1365-3121.1991.tb00873.x

Anderson, J. A., & Wood, H. O. (1925). Description and theory of the torsion seismometer. *Bulletin of the Seismological Society of America*, *15*(1), 1–72.

Barry, P. H., Hilton, D. R., Fischer, T. P., de Moor, J. M., Mangasini, F., & Ramirez, C. (2013). Helium and carbon isotope systematics of cold "mazuku" CO_2 vents and hydrothermal gases and fluids from Rungwe Volcanic Province, southern Tanzania. *Chemical Geology*, *339*, 141–156. https://doi.org/10.1016/j.chemgeo.2012.07.003

Behn, M. D., Conrad, C. P., & Silver, P. G. (2004). Detection of upper mantle flow associated with the African Superplume. *Earth and Planetary Science Letters*, *224*(3-4), 259–274. https://doi.org/10.1016/j.epsl.2004.05.026

Biggs, J., Nissen, E., Craig, T., Jackson, J., & Robinson, D. P. (2010). Breaking up the hanging wall of a rift-border fault: The 2009 Karonga earthquakes, Malawi. *Geophysical Research Letters*, *37*, L11305. https://doi.org/10.1029/2010GL043179

Bilek, S. L., & Lay, T. (2018). Subduction zone megathrust earthquakes. *Geosphere*, *14*(4), 1468–1500. https://doi.org/10.1130/GES01608.1

Boniface, N., & Appel, P. (2018). Neoproterozoic reworking of the Ubendian Belt crust: Implication for an orogenic cycle between the Tanzania Craton and Bangweulu Block during the assembly of Gondwana. *Precambrian Research*, *305*(December 2017), 358–385. https://doi.org/10.1016/j.precamres.2017.12.011

Borrego, D., Nyblade, A. A., Accardo, N. J., Gaherty, J. B., Ebinger, C. J., Shillington, D. J., et al. (2018). Crustal structure surrounding the northern Malawi rift and beneath the Rungwe Volcanic Province, East Africa. *Geophysical Journal International*, *215*(2), 1410–1426. https://doi.org/10.1093/gji/ggy331

Braun, J., & Beaumont, C. (1989). A physical explanation of the relation between flank uplifts and the breakup unconformity at rifted continental margins. *Geology*, *17*(8), 760–764. https://doi.org/10.1130/0091-7613(1989)017<0760:APEOTR>2.3.CO;2

Brazier, R. A., Nyblade, A. A., & Florentin, J. (2005). Focal mechanisms and the stress regime in NE and SW Tanzania, East Africa. *Geophysical Research Letters*, *32*, L14315. https://doi.org/10.1029/2005GL023156

Buck, W. R. (2004). Consequences of asthenospheric variability on continental rifting. In *Rheology and deformation of the lithosphere at continental margins* (Vol. 62, pp. 1–30). New York: Columbia University Press.

Burov, E., Jaupart, C., & Guillou-Frottier, L. (2003). Ascent and emplacement of buoyant magma bodies in brittle-ductile upper crust. *Journal of Geophysical Research - Solid Earth*, *108*(B4). https://doi.org/10.1029/2002JB001904

Camelbeeck, T., & Iranga, M. D. (1996). Deep crustal earthquakes and active faults along the Rukwa trough, eastern Africa. *Geophysical Journal International*, *124*(2), 612–630. https://doi.org/10.1111/j.1365-246X.1996.tb07040.x

Castaing, C. (1991). Post-Pan-African tectonic evolution of South Malawi in relation to the Karroo and recent East African rift systems. *Tectonophysics*, *191*(1–2), 55–73. https://doi.org/10.1016/0040-1951(91)90232-H.

Chorowicz, J. (2005). The east African rift system. *Journal of African Earth Sciences*, *43*(1-3), 379–410. https://doi.org/10.1016/j.jafrearsci.2005.07.019

Condori, C., Tavera, H., Marotta, G. S., Rocha, M. P., & França, G. S. (2017). Calibration of the local magnitude scale (ML) for Peru. *Journal of Seismology*, *21*(4), 987–999. https://doi.org/10.1007/s10950-017-9647-3

Craig, T. J., Jackson, J. A., Priestley, K., & McKenzie, D. (2011). Earthquake distribution patterns in Africa: their relationship to variations in lithospheric and geological structure, and their rheological implications. *Geophysical Journal International*, *185*(1), 403–434. Retrieved from. https://doi.org/10.1111/j.1365-246X.2011.04950.x

Crossley, R. (1984). Controls of sedimentation in the Malawi rift valley, central Africa. *Sedimentary Geology*, *40*(1-3), 33–50. https://doi.org/10.1016/0037-0738(84)90038-1

Dahm, T., Heimann, S., Funke, S., Wendt, S., Rappsilber, I., Bindi, D., et al. (2018). Seismicity in the block mountains between Halle and Leipzig, Central Germany: Centroid moment tensors, ground motion simulation, and felt intensities of two $M \approx 3$ earthquakes in 2015 and 2017. *Journal of Seismology*, *22*(4), 985–1003. https://doi.org/10.1007/s10950-018-9746-9

Delvaux, D. (2001). Tectonic and palaeostress evolution of the Tanganyika-Rukwa-Malawi rift segment, East African rift System. *Peri-Tethys Memoir*, *6*, 545–567.

Delvaux, D., & Barth, A. (2010). African stress pattern from formal inversion of focal mechanism data. *Tectonophysics*, *482*(1–4), 105–128. https://doi.org/10.1016/J.TECTO.2009.05.009

Dziewonski, A. M., Chou, T.-A., & Woodhouse, J. H. (1991). Determination of earthquake source parameters from waveform data for studies of global and regional seismicity. *Journal of Geophysical Research*, *86*(B4), 2825–2852. https://doi.org/10.1029/JB086iB04p02825

Ebinger, C., Deino, A., Drake, R., & Tesha, A. (1989). Chronology of volcanism and rift basin propagation, Rungwe province, East Africa. *Journal of Geophysical Research*, *94*(B11), 15,785–15,803. https://doi.org/10.1029/JB094iB11p15785

Ebinger, C. J., & Casey, M. (2001). Continental breakup in magmatic provinces: An Ethiopian example. *Geology*, *29*(6), 527–530. https://doi.org/10.1130/0091-7613(2001)029<0527:CBIMPA>2.0.CO;2

Ebinger, C. J., Karner, G. D., & Weissel, J. K. (1991). Mechanical strength of extended continental lithosphere: Constraints from the Western Rift System, East Africa. *Tectonics*, *10*(6), 1239–1256. https://doi.org/10.1029/91TC00579

Ebinger, C. J., Keir, D., Bastow, I. D., Whaler, K. A., Hammond, J. O. S., Ayele, A., et al. (2017). Crustal structure of active deformation zones in Africa: Implications for global crustal processes. *Tectonics*, *36*, 3298–3332. https://doi.org/10.1002/2017TC004526

Ekström, G., Nettles, M., & Dziewonski, A. M. (2012). The global CMT project 2004-2010: Centroid-moment tensors for 13,017 earthquakes. *Physics of the Earth and Planetary Interiors*, *200-201*, 1–9. https://doi.org/10.1016/j.pepi.2012.04.002

Ellis, M., & King, G. (1991). Structural control of flank volcanism in continental rifts. *Science*, *254*(5033), 839 LP-842. Retrieved from). http://science.sciencemag.org/content/254/5033/839.abstract

Fagereng, Å. (2013). Fault segmentation, deep rift earthquakes and crustal rheology: Insights from the 2009 Karonga sequence and seismicity in the Rukwa–Malawi rift zone. *Tectonophysics*, *601*, 216–225. https://doi.org/10.1016/j.tecto.2013.05.012

Fishwick, S., & Bastow, I. D. (2011). Towards a better understanding of African topography: a review of passive-source seismic studies of the African crust and upper mantle. *Geological Society, London, Special Publications*, *357*(1), 343–371. https://doi.org/10.1144/sp357.19

Fontijn, K., Williamson, D., Mbede, E., & Ernst, G. G. (2012). The Rungwe volcanic province, Tanzania–a volcanological review. *Journal of African Earth Sciences*, *63*, 12–31. https://doi.org/10.1016/j.jafrearsci.2011.11.005

Foster, A. N., & Jackson, J. A. (1998). Source parameters of large African earthquakes: implications for crustal rheology and regional kinematics. *Geophysical Journal International*, *134*(2), 422–448. Retrieved from. https://doi.org/10.1046/j.1365-246x.1998.00568.x

Fritz, H., Abdelsalam, M., Ali, K. A., Bingen, B., Collins, A. S., Fowler, A. R., et al. (2013). Orogen styles in the East African Orogen: A review of the Neoproterozoic to Cambrian tectonic evolution. *Journal of African Earth Sciences*, *86*, 65–106. https://doi.org/10.1016/J.JAFREARSCI.2013.06.004

Frohlich, C. (1994). Earthquakes with non-double-couple mechanisms. *Science*, *264*(5160), 804–809. https://doi.org/10.1126/science.264.5160.804

Furman, T. (1995). Melting of metasomatized subcontinental lithosphere: undersaturated mafic lavas from Rungwe, Tanzania. *Contributions to Mineralogy and Petrology*, *122*(1-2), 97–115. https://doi.org/10.1007/s004100050115

Gaherty, J., Ebinger, C. J., Nyblade, A. A., & Shillington, D. J. (2013). Study of Extension and maGmatism in Malawi aNd Tanzania. *International Federation of Digital Seismograph Networks. Other/Seismic Network*. https://doi.org/10.7914/SN/YQ_2013

Gaherty, J., Zheng, W., Shillington, D. J., Pritchard, M. E., Henderson, S. T., Chindandali, P. R. N., et al. (2019). Faulting processes during early-stage rifting: seismic and geodetic analysis of the 2009-2010 Northern Malawi earthquake sequence. *Geophysical Journal International*, *217*(3), 1767–1782. https://doi.org/10.1093/gji/ggz119

Gasperini, P., Lolli, B., & Vannucci, G. (2013). Body wave magnitude mb is a good proxy of moment magnitude Mw for small earthquakes (mb<4.5–5.0). *Seismological Research Letters*, *84*(6), 932–937. https://doi.org/10.1785/0220130105

Grijalva, A., Nyblade, A. A., Homman, K., Accardo, N. J., Gaherty, J. B., Ebinger, C. J., et al. (2018). Seismic evidence for plume-and craton-influenced upper mantle structure beneath the northern Malawi rift and the Rungwe volcanic province, East Africa. *Geochemistry, Geophysics, Geosystems*, *19*(10), 3980–3994. https://doi.org/10.1029/2018GC007730

Gupta, H. K. (1992). The Malawi earthquake of March 10, 1989: a report of the macroseismic survey. *Tectonophysics*, *209*(1-4), 165–166. https://doi.org/10.1016/0040-1951(92)90018-2

Gutenberg, B., & Richter, C. F. (1954). *Seismicity of the earth and related phenomena*. Princeton (NJ): Princeton University Press.

Halldórsson, S. A., Hilton, D. R., Scarsi, P., Abebe, T., & Hopp, J. (2014). A common mantle plume source beneath the entire East African Rift System revealed by coupled helium-neon systematics. *Geophysical Research Letters*, *41*, 2304–2311. https://doi.org/10.1002/2014GL059424

Hardebeck, J. L., & Michael, A. J. (2006). Damped regional-scale stress inversions: Methodology and examples for southern California and the Coalinga aftershock sequence. *Journal of Geophysical Research - Solid Earth*, *111*(B11). https://doi.org/10.1029/2005JB004144

Harper, R. M., Morley, C. K., & Stone, D. M. (1999). Geophysics of the Usangu Flats, Tanzania. In C. K. Morley (Ed.), *Geoscience of rift systems—Evolution of East Africa*, *AAPG Studies in Geology No. 44*, (pp. 111–114).

Heimann, S., Isken, M., Kühn, D., Sudhaus, H., Steinberg, A., Vasyura-Bathke, H., et al. (2018). Grond—A probabilistic earthquake source inversion framework. V. 1.0. GFZ Data Services. https://doi.org/10.5880/GFZ.2.1.2018.003

Heimann, S., Kriegerowski, M., Isken, M., Cesca, S., Daout, S., Grigoli, F., et al. (2017). Pyrocko—An open-source seismology toolbox and library. https://doi.org/10.5880/GFZ.2.1.2017.001

Hellebrekers, N., Niemeijer, A., Fagereng, A., Manda, B., & Mvula, R. (2019, June 5). Lower crustal earthquakes in the East African Rift System: Insights from frictional properties of rock samples from the Malawi rift. https://doi.org/10.31223/osf.io/nu7rq

Hicks, S. P., & Rietbrock, A. (2015). Seismic slip on an upper-plate normal fault during a large subduction megathrust rupture. *Nature Geoscience*, *8*(12), 955–960. https://doi.org/10.1038/ngeo2585

Hilbert-Wolf, H., Roberts, E., Downie, B., Mtelela, C., Stevens, N. J., & O'Connor, P. (2017). Application of U–Pb detrital zircon geochronology to drill cuttings for age control in hydrocarbon exploration wells: A case study from the Rukwa Rift Basin, Tanzania. *AAPG Bulletin*, *101*(02), 143–159. https://doi.org/10.1306/06281616003

Hodge, M., Biggs, J., Goda, K., & Aspinall, W. (2015). Assessing infrequent large earthquakes using geomorphology and geodesy: the Malawi Rift. *Natural Hazards*, *76*(3), 1781–1806. https://doi.org/10.1007/s11069-014-1572-y

Hodgson, I., Illsley-Kemp, F., Gallacher, R. J., Keir, D., Ebinger, C. J., & Mtelela, K. (2017). Crustal structure at a young continental rift: A receiver function study from the Tanganyika Rift. *Tectonics*, *36*, 2806–2822. https://doi.org/10.1002/2017TC004477

Hutton, L. K., & Boore, D. M. (1987). The ML scale in Southern California. *Bulletin of the Seismological Society of America*, *77*(6), 2074–2094.

Illsley-Kemp, F., Keir, D., Bull, J. M., Ayele, A., Hammond, J. O. S., Kendall, J. -M., et al. (2017). Local earthquake magnitude scale and *b*-value for the Danakil Region of Northern Afar. *Bulletin of the Seismological Society of America*, *107*(2), 521–531. https://doi.org/10.1785/0120150253

Jackson, J., & Blenkinsop, T. (1993). The Malaŵi earthquake of March 10, 1989: Deep faulting within the East African Rift System. *Tectonics*, *12*(5), 1131–1139. https://doi.org/10.1029/93TC01064

Kaaya, C. Z. (1992). Depositional environment of Late Permian Karoo beds in the Ruhuhu Basin and Mikumi area of Tanzania (No. 83). PhD thesis, Geologisches Institut, Universität zu Köln.

Keir, D., Stuart, G. W., Jackson, A., & Ayele, A. (2006). Local earthquake magnitude scale and seismicity rate for the Ethiopian rift. *Bulletin of the Seismological Society of America*, *96*(6), 2221–2230.

Kissling, E. (1988). Geotomography with local earthquake data. *Reviews of Geophysics*, *26*(4), 659–698. https://doi.org/10.1029/RG026i004p00659

Kissling, E., Kradolfer, U., & Maurer, H. (1995). *Program VELEST user's guide-Short Introduction*. ETH Zurich: Institute of Geophysics.

Klein, F. W. (2002). User's guide to HYPOINVERSE-2000, a Fortran program to solve for earthquake locations and magnitudes. *U.S. Geol. Surv. Open File Report 02-171*, 123 pp. https://doi.org/http://geopubs.wr.usgs.gov/open-file/of02-171/

Kolawole, F., Atekwana, E. A., Laó-Dávila, D. A., Abdelsalam, M. G., Chindandali, P. R., Salima, J., & Kalindekafe, L. (2018a). Active deformation of Malawi rift's North Basin Hinge Zone modulated by reactivation of preexisting Precambrian shear zone fabric. *Tectonics*, *37*(3), 683–704. https://doi.org/10.1002/2017TC004628

Kolawole, F., Atekwana, E. A., Laó-Dávila, D. A., Abdelsalam, M. G., Chindandali, P. R., Salima, J., & Kalindekafe, L. (2018b). High-resolution electrical resistivity and aeromagnetic imaging reveal the causative fault of the 2009 M w 6.0 Karonga, Malawi earthquake. *Geophysical Journal International*, *213*(2), 1412–1425. https://doi.org/10.1093/gji/ggy066

Kostrov, V. V. (1974). Seismic moment and energy of earthquakes, and seismic flow of rock. *Izv. Acad. Sci. USSR Phys. Solid Earth*, *1*, 23–44.

Langston, C. A., Brazier, R., Nyblade, A. A., & Owens, T. J. (1998). Local magnitude scale and seismicity rate for Tanzania, East Africa. *Bulletin of the Seismological Society of America*, *88*(3), 712–721.

Lavayssière, A., Drooff, C., Ebinger, C., Gallacher, R., Illsley-Kemp, F., Oliva, S. J., & Keir, D. (2019). Depth Extent and Kinematics of Faulting in the Southern Tanganyika Rift, Africa. *Tectonics*, *38*(3), 842–862. https://doi.org/10.1029/2018TC005379

Lavier, L. L., & Buck, W. R. (2002). Half graben versus large-offset low-angle normal fault: Importance of keeping cool during normal faulting. *Journal of Geophysical Research - Solid Earth*, *107*(B6), ETG-8. https://doi.org/10.1029/2001JB000513

Lithgow-Bertelloni, C., & Silver, P. G. (1998). Dynamic topography, plate driving forces and the African superswell. *Nature*, *395*(6699), 269.

Lloyd, F. E., Arima, M., & Edgar, A. D. (1985). Partial melting of a phlogopite-clinopyroxenite nodule from south-west Uganda: An experimental study bearing on the origin of highly potassic continental rift volcanics. *Contributions to Mineralogy and Petrology*, *91*(4), 321–329. https://doi.org/10.1007/BF00374688

Maguire, P. K. H., Swain, C. J., Masotti, R., & Khan, M. A. (1994). A crustal and uppermost mantle cross-sectional model of the Kenya Rift derived from seismic and gravity data. *Tectonophysics*, *236*(1-4), 217–249. https://doi.org/10.1016/0040-1951(94)90178-3

Martínez-Garzón, P., Kwiatek, G., Ickrath, M., & Bohnhoff, M. (2014). MSATSI: A MATLAB package for stress inversion combining solid classic methodology, a new simplified user-handling, and a visualization tool. *Seismological Research Letters*, *85*(4), 896–904. Retrieved from. https://doi.org/10.1785/0220130189

Mbede, E. I. (2002). Interpretation of reflection seismic data from the Usangu Basin, East African Rift System. *Tanzania Journal of Science*, *28*, 83–97. https://doi.org/10.4314/tjs.v28i1.18321

McCartney, T., & Scholz, C. A. (2016). A 1.3 million year record of synchronous faulting in the hangingwall and border fault of a half-graben in the Malawi (Nyasa) Rift, J. *Structural Geology*, *91*, 114–129. https://doi.org/10.1016/j.jsg.2016.08.012

Mechie, J., Keller, G. R., Prodehl, C., Gaciri, S., Braile, L. W., Mooney, W. D., et al. (1994). Crustal structure beneath the Kenya Rift from axial profile data. *Tectonophysics*, *236*(1-4), 179–200. https://doi.org/10.1016/0040-1951(94)90176-7

Mesko, G. T., Class, C., Maqway, M. D., Boniface, N., Manya, S., & Hemming, S. R. (2014). The Timing of early magmatism and extension in the southern East African Rift: Tracking geochemical source variability with 40Ar/39Ar geochronology at the Rungwe Volcanic Province, SW Tanzania. In *AGU Fall Meeting Abstracts*.

Midzi, V., Hlatywayo, D. J., Chapola, L. S., Kebede, F., Atakan, K., Lombe, D. K., et al. (1999). Seismic hazard assessment in Eastern and Southern Africa. *Annals of Geophysics*, *42*(6).

Morley, C. K., Nelson, R. A., Patton, T. L., & Munn, S. G. (1990). Transfer zones in the East African rift system and their relevance to hydrocarbon exploration in rifts (1). *AAPG Bulletin*, *74*(8), 1234–1253.

Mortimer, E., Paton, D. A., Scholz, C. A., Strecker, M. R., & Blisniuk, P. (2007). Orthogonal to oblique rifting: effect of rift basin orientation in the evolution of the North basin, Malawi Rift, East Africa. *Basin Research*, *19*(3), 393–407. https://doi.org/10.1111/j.1365-2117.2007.00332.x

Mulibo, G. D., & Nyblade, A. A. (2013). The *P* and *S* wave velocity structure of the mantle beneath eastern Africa and the African superplume anomaly. *Geochemistry, Geophysics, Geosystems*, *14*, 2696–2715. https://doi.org/10.1002/ggge.20150

Nyblade, A. A., & Robinson, S. W. (1994). The African Superswell. *Geophysical Research Letters*, *21*(9), 765–768. https://doi.org/10.1029/94GL00631

O'Donnell, J. P., Selway, K., Nyblade, A. A., Brazier, R. A., Tahir, N. E., & Durrheim, R. J. (2015). Thick lithosphere, deep crustal earthquakes and no melt: A triple challenge to understanding extension in the western branch of the East African Rift. *Geophysical Journal International*, *204*(2), 985–998. https://doi.org/10.1093/gji/ggv492

Oliva, S. J., Ebinger, C. J., Wauthier, C., Muirhead, J. D., Roecker, S. W., Rivalta, E., & Heimann, S. (2019). Insights into fault-magma interactions in an early-stage continental rift from source mechanisms and correlated volcano-tectonic earthquakes. *Geophysical Research Letters*, *46*(4), 2065–2074. https://doi.org/10.1029/2018GL080866

Olive, J. A., Behn, M. D., & Malatesta, L. C. (2014). Modes of extensional faulting controlled by surface processes. *Geophysical Research Letters*, *41*, 6725–6733. https://doi.org/10.1002/2014GL061507

Pérez-Gussinyé, M., Metois, M., Fernández, M., Vergés, J., Fullea, J., & Lowry, A. R. (2009). Effective elastic thickness of Africa and its relationship to other proxies for lithospheric structure and surface tectonics. *Earth and Planetary Science Letters*, *287*(1-2), 152–167. https://doi.org/10.1016/j.epsl.2009.08.004

Rasskazov, S. V., Logachev, N. A., Ivanov, A. V., Boven, A. A., Maslovskaya, M. N., Saranina, E. V., et al. (2001). The 19-17 ma magmatic episode in the Western rift of East Africa and its bearing on geodynamics. *Doklady Akademii Nauk-Rossijskaya Akademiya Nauk*, *381*(2), 230–233.

Reyes, C. G., & West, M. E. (2011). The waveform suite: A robust platform for manipulating waveforms in MATLAB. *Seismological Research Letters*, *82*(1), 104–110. https://doi.org/10.1785/gssrl.82.1.104

Richter, C. F. (1935). An instrumental earthquake magnitude scale. *Bulletin of the Seismological Society of America*, *25*(1), 1–32.

Ring, U. (1994). The influence of preexisting structure on the evolution of the Cenozoic Malawi rift (East African rift system). *Tectonics*, *13*(2), 313–326. https://doi.org/10.1029/93TC03188

Saria, E., Calais, E., Stamps, D. S., Delvaux, D., & Hartnady, C. J. H. (2014). Present-day kinematics of the East African Rift. *Journal of Geophysical Research: Solid Earth*, *119*, 3584–3600. https://doi.org/10.1002/2013JB010901

Scholz, C. A., & Lyons, R. P. (2010). New age estimates for the Lake Malawi Rift, East Africa, using deep scientific drill cores and seismic reflection data. In *AGU Fall Meeting Abstracts*.

Scholz, C. H. (1968). The frequency-magnitude relation of microfracturing in rock and its relation to earthquakes. *Bulletin of the Seismological Society of America*, *58*(1), 399–415.

Scholz, C. H. (2015). On the stress dependence of the earthquake b value. *Geophysical Research Letters*, *42*, 1399–1402. https://doi.org/10.1002/2014GL062863

Snoke, J. A. (1984). A program for focal mechanism determination by combined use of polarity and SV-P amplitude ratio data. *Earthquake Notes*, *55*, 15.

Stamps, D. S., Saria, E., & Kreemer, C. (2018). A geodetic strain rate model for the East African Rift System. *Scientific Reports*, *8*(1), 732. https://doi.org/10.1038/s41598-017-19097-w

Stockley, G. M. (1931). Report on the geology of the Ruhuhu coalfields. *Geological Survey of Tanganyika, Bulletin*, *2*, 1–68.

Tepp, G., Ebinger, C. J., Zal, H., Gallacher, R. J., Accardo, N. J., Shillington, D. J., et al. (2018). Seismic anisotropy of the upper mantle below the Western Rift, East Africa. *Journal of Geophysical Research: Solid Earth*, *123*(7), 5644–5660. https://doi.org/10.1029/2017JB015409

Tiercelin, J. J., Chorowicz, J., Bellon, H., Richert, J. P., Mwanbene, J. T., & Walgenwitz, F. (1988). East African rift system: offset, age and tectonic significance of the Tanganyika-Rukwa-Malawi intracontinental transcurrent fault zone. *Tectonophysics*, *148*(3–4), 241–252. https://doi.org/10.1016/0040-1951(88)90133-3

Tongue, J., Maguire, P., & Burton, P. (1994). An earthquake study in the Lake Baringo basin of the central Kenya Rift. *Tectonophysics*, *236*(1–4), 151–164. https://doi.org/10.1016/0040-1951(94)90174-0

Tormann, T., Enescu, B., Woessner, J., & Wiemer, S. (2015). Randomness of megathrust earthquakes implied by rapid stress recovery after the Japan earthquake. *Nature Geoscience*, *8*(2), 152–158. https://doi.org/10.1038/ngeo2343

Vavryčuk, V. (2014). Iterative joint inversion for stress and fault orientations from focal mechanisms. *Geophysical Journal International*, *199*(1), 69–77. Retrieved from. https://doi.org/10.1093/gji/ggu224

Waldhauser, F. (2001). hypoDD--A program to compute double-difference hypocenter locations (hypoDD version 1.0-03/2001). *US Geol. Surv. Open File Rep., 01*, *113*.

Waldhauser, F., & Ellsworth, W. L. (2000). A double-difference earthquake location algorithm: Method and application to the northern Hayward fault, California. *Bulletin of the Seismological Society of America*, *90*(6), 1353–1368. https://doi.org/10.1785/0120000006

Wang, H., Hunen, J., & Graham Pearson, D. (2015). The thinning of subcontinental lithosphere: The roles of plume impact and metasomatic weakening. *Geochemistry, Geophysics, Geosystems*, *16*, 1156–1171. https://doi.org/10.1002/2015GC005784

Wang, Q., & Ji, S. (2009). Poisson's ratios of crystalline rocks as a function of hydrostatic confining pressure. *Journal of Geophysical Research*, *114*(B9). https://doi.org/10.1029/2008JB006167

Wang, R. (1999). A simple orthonormalization method for stable and efficient computation of Green's functions. *Bulletin of the Seismological Society of America*, *89*(3), 733–741.

Watts, A., & Burov, E. (2003). Lithospheric strength and its relationship to the elastic and seismogenic layer thickness. *Earth and Planetary Science Letters*, *213*(1–2), 113–131. https://doi.org/10.1016/S0012-821X(03)00289-9

Weinstein, A., Oliva, S. J., Ebinger, C. J., Roecker, S., Tiberi, C., Aman, M., et al. (2017). Fault-magma interactions during early continental rifting: Seismicity of the Magadi-Natron-Manyara basins, Africa. *Geochemistry, Geophysics, Geosystems*, *18*, 3662–3686. https://doi.org/10.1002/2017GC007027

Weissel, J. K., & Karner, G. D. (1989). Flexural uplift of rift flanks due to mechanical unloading of the lithosphere during extension. *Journal of Geophysical Research - Solid Earth*, *94*(B10), 13,919–13,950. https://doi.org/10.1029/JB094iB10p13919

Woessner, J., & Wiemer, S. (2005). Assessing the quality of earthquake catalogues: Estimating the magnitude of completeness and its uncertainty. *Bulletin of the Seismological Society of America*, *95*(2), 684–698. https://doi.org/10.1785/012004000

Wood, D. A., Zal, H. J., Scholz, C. A., Ebinger, C. J., & Nizère, I. (2017). Evolution of the Kivu Rift, East Africa: Interplay among tectonics, sedimentation and magmatism. *Basin Research*, *29*, 175–188. https://doi.org/10.1111/bre.12143

Yang, Z., & Chen, W. P. (2008). Mozambique earthquake sequence of 2006: High-angle normal faulting in southern Africa. *Journal of Geophysical Research - Solid Earth*, *113*(B12). https://doi.org/10.1029/2007JB005419

Yang, Z., & Chen, W. P. (2010). Earthquakes along the East African Rift System: A multiscale, system-wide perspective. *Journal of Geophysical Research - Solid Earth*, *115*(B12). https://doi.org/10.1029/2009JB006779